Nano Materials Science 1 (2019) 31–47

Contents lists available at ScienceDirect

Nano Materials Science

journal homepage: www.keaipublishing.com/cn/journals/nano-materials-science/

Synthesis, properties, and applications of graphene oxide/reduced graphene oxide and their nanocomposites

Andrew T. Smith [a,b,1], Anna Marie LaChance [a,b,1], Songshan Zeng [a,b], Bin Liu [c], Luyi Sun [a,b,d,*]

[a] Polymer Program, Institute of Materials Science, University of Connecticut, Storrs, Connecticut, 06269, United States
[b] Department of Chemical and Biomolecular Engineering, University of Connecticut, Storrs, Connecticut, 06269, United States
[c] College of Materials Science and Engineering, Beijing University of Chemical Technology, Beijing, 100029, China
[d] Department of Biomedical Engineering, University of Connecticut, Storrs, Connecticut, 06269, United States

ARTICLE INFO

Keywords:
Graphene oxide
Reduced graphene oxide
Graphene quantum dots polymer
Nanocomposites
Synthesis
Properties of graphene and graphene oxide
Applications

ABSTRACT

Thanks to their remarkable mechanical, electrical, thermal, and barrier properties, graphene-based nanocomposites have been a hot area of research in the past decade. Because of their simple top-down synthesis, graphene oxide (GO) and reduced graphene oxide (rGO) have opened new possibilities for gas barrier, membrane separation, and stimuli-response characteristics in nanocomposites. Herein, we review the synthesis techniques most commonly used to produce these graphene derivatives, discuss how synthesis affects their key material properties, and highlight some examples of nanocomposites with unique and impressive properties. We specifically highlight their performances in separation applications, stimuli-responsive materials, anti-corrosion coatings, and energy storage. Finally, we discuss the outlook and remaining challenges in the field of practical industrial-scale production and use of graphene-derivative-based polymer nanocomposites.

1. Introduction

Graphene is an atomically-thin, 2-dimensional (2D) sheet of sp^2 carbon atoms in a honeycomb structure. It has been shown to have many desirable properties such as high mechanical strength [1], electrical conductivity [2], molecular barrier abilities [3] and other remarkable properties. For these reasons, it has been the goal of countless research efforts to incorporate graphene into polymers to design polymer-based nanocomposites [4–7]. However, the use of pristine graphene has proved challenging due to difficult bottom-up synthesis [8], poor solubility [9], and agglomeration in solution due to van der Waals interactions [2]. As an alternative, compounds similar in structure to graphene can be synthesized from graphite or other carbon sources by a top-down method in an effort to achieve many of the advantages of pristine graphene while also imbuing the surface with functionalized oxygen groups. The oxidation of graphite in protonated solvents leads to graphite oxide, which consists of multiple stacked layers of graphene oxide (GO).

GO has a similar hexagonal carbon structure to graphene but also contains hydroxyl (—OH), alkoxy (C—O—C), carbonyl (C═O), carboxylic acid (—COOH) and other oxygen-based functional groups [10]. Aside from the ease of synthesis, these oxygenated groups are responsible for many advantages over graphene, including higher solubility [2] and the possibility for surface functionalization which have presented many opportunities for use in nanocomposite materials. Furthermore, GO can be treated by a number of methods to synthesize reduced graphene oxide (rGO) in efforts to minimize the number of oxygen groups and achieve properties closer to those of pristine graphene [11]. Recently, another class of graphene derivative has emerged known as graphene quantum dots (GQDs) which are essentially graphene sheets of <100 nm in their lateral dimension; these take advantage of the unique edge effects of graphene.

Graphene derivatives (GO, rGO, GQDs) have proven to be effective fillers in polymer nanocomposite materials thanks to their ideal material properties and dispersibility in polymer matrices [12,13], which has led to many applications. The tight packing of sp^2 carbon atoms has been shown to serve as a near-perfect barrier to gas molecules [3,14], which demonstrates its use in packaging materials [12], protection for sensitive electronic devices [14], or even corrosion-resistant materials [15,16]. For similar reasons, the fine-tuning of the filler content in nanocomposites can be used to adjust the selectivity of certain-sized molecules to generate superior membrane technologies [17,18]. Furthermore, the

* Corresponding author. Polymer Program, Institute of Materials Science, University of Connecticut, Storrs, Connecticut, 06269, United States.
E-mail address: luyi.sun@uconn.edu (L. Sun).
[1] These authors contributed equally to this work.

https://doi.org/10.1016/j.nanoms.2019.02.004
Received 21 January 2019; Accepted 22 February 2019
Available online 23 March 2019

unique hydrophilic, thermal, and electrical properties of GO can be taken advantage of in stimuli-responsive materials [19–21]. This review aims to summarize the synthesis techniques, unique material properties (mechanical, electrical, thermal, etc.), and some representative applications (coating, membrane, anti-corrosion, and stimuli-responsiveness) of functional GO/rGO nanocomposite materials.

2. Synthesis

When considering the synthesis of graphene and its derivatives, the desired structure and properties are largely dependent upon the size, shape, and functional groups attached to the surface of the material. The ideal structure is single layer graphene consisting of a single-atom-thin fully sp^2 hybridized carbon structure with minimal defects (Fig. 1A). However, due to the highly favorable stacking of graphene sheets, a multi-layered structure of graphene (Fig. 1B) will also be generated. As mentioned above, the synthesis of these structures with a bottom-up approach has proven difficult for industrial applications. As such, with a top-down approach, it is easier to generate the highly oxidized form of graphene, GO, with both sp^2 and sp^3 carbon containing abundant oxygen groups (Fig. 1C), which upon reduction (rGO) can eliminate most of the oxygen groups and sp^3 carbon to generate a more graphene-"like" material with much-improved properties (Fig. 1D). Both GO and rGO can be then processed further through the top-down approach to produce quantum dots of both GOQD and rGQD (Fig. 1E and F). In the following sections, the current approaches to synthesizing the aforementioned materials will be discussed.

2.1. Synthesis of GO

The synthesis of GO can essentially be divided into two main categories: bottom-up methods where simple carbon molecules are used to construct pristine graphene, and "top-down" methods where layers of graphene derivatives are extracted from a carbon source, typically graphite [22,23]. Bottom-up synthesis (such as chemical vapor deposition, epitaxial growth on silicon carbide wafers, etc.) has been shown to be time-consuming and faces challenges to scalability [24]. Hence, the focus on top-down methods, which first generate GO and/or rGO, are more popular for realizing graphene derivatives, particularly for use in nanocomposite materials. The first synthesis of GO is often attributed to Brodie, [25] Staudenmaier [26], and Hummers and Offeman [27], each of whom derived graphite oxide via the oxidation of graphite using various techniques. Hummers and Offeman made a number of improvements on the original two techniques to make them safer, including

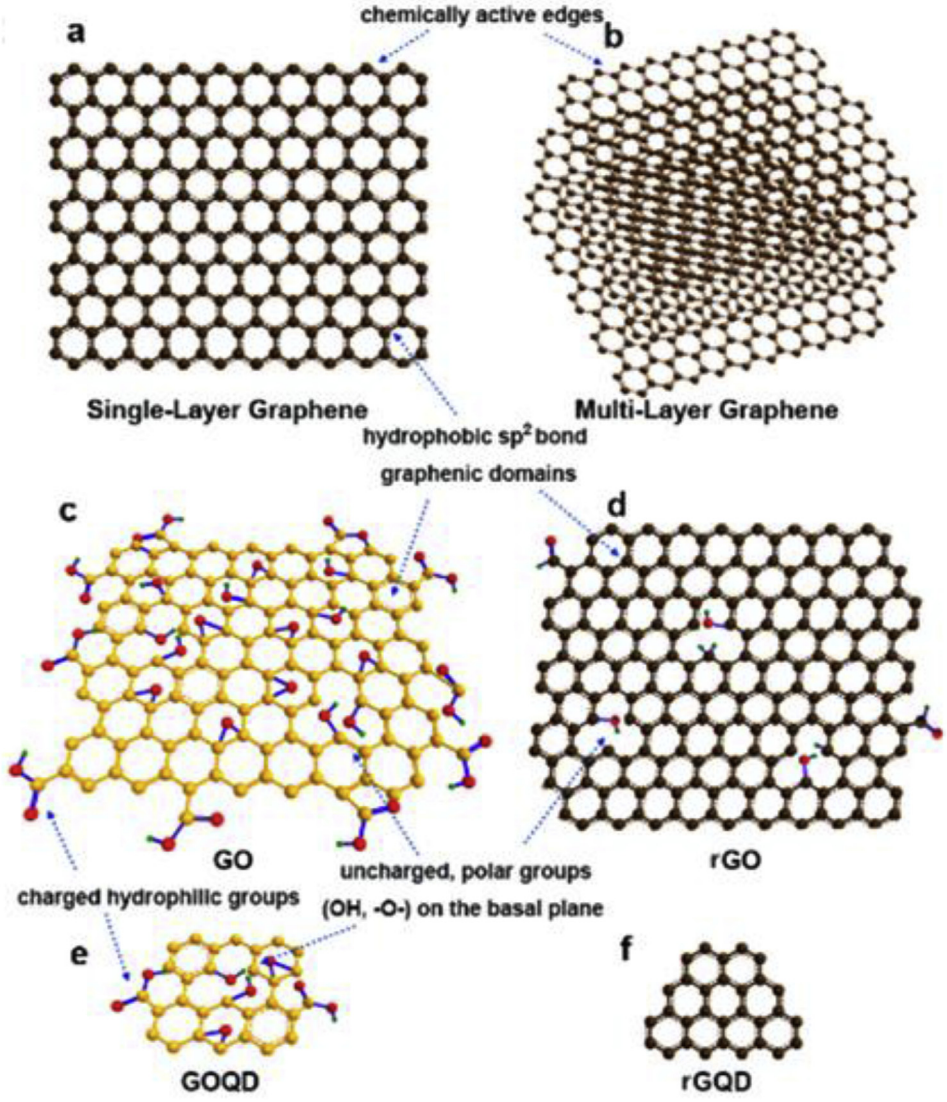

Fig. 1. Forms of graphene and its derivatives: (A) single-layer graphene, (B) multilayer graphene, (C) GO, (D) rGO, (E) GOQD, (F) rGQD. Modified with permission from the American Chemical Society [13].

the use of $KMnO_4$ as an oxidizer (rather than $KClO_3$, which evolves toxic ClO_2 gas) and the addition of sodium nitrate (to form nitric acid in situ rather than using nitric acid as a solvent). Due to the safer and more scalable nature of the Hummers' method, this is the one that is generally used (or, in most cases, slightly altered) to generate GO.

Any method which changes or improves upon the synthesis route proposed by Hummers is regarded ubiquitously as a "modified Hummers method", however the exact meaning of this term is far from standardized [10]. In general, a carbon source (often graphite flakes or powders) is put into a protonated solvent (such as sulfuric acid, phosphoric acid, or some mixture of these) and a strong oxidizing agent (usually $KMnO_4$) is introduced. Following a dilution step, it is common to treat the resulting mixture with H_2O_2 to remove any metal ions from the oxidizer; this results in a yellow bubbling and ultimately a yellow-brown liquid. The resulting solids are then separated and treated with dilute hydrochloric acid to further remove any metal species, and the solution is washed and centrifuged several times with water until the pH of the solution is essentially neutral.

The overall synthesis route can be modified to fit an individual researcher's needs. For instance, it is worth noting that the size and shape of the carbon source will determine the size and shape of the resulting graphene oxide via a modified Hummer's method [10]. Typically, this means that the average diameter of the graphite powders used in synthesis will determine the average lateral dimension of the resulting GO sheets, although other carbon sources can be used. In one interesting example, Huang et al. [28] synthesized long, thin strips of GO (which they call "GO nanoribbons") by unzipping multi-walled carbon nanotubes. Graphite can also be oxidized prior to GO synthesis to decrease the C/O ratio of the final product. Many labs use the method proposed by Kovtyukhova et al. [29], which pre-treats graphite powders in $K_2S_2O_8$ and P_2O_5 prior to use in the Hummers' method [2,11,12]. Other researchers modify graphite into expanded graphite by thermal treatment or exposure to strong oxidizers to increase the interlayer spacing of the carbon source, resulting in easier delamination of the graphite oxide layers [30,31]. Another popular modification of this technique is the "improved Hummers' method", which removes sodium nitride with the addition of phosphoric acid and an increased amount of $KMnO_4$. This improvement evolves no toxic gases, provides easy temperatures control, and results in GO powders with a higher degree of oxidation [32]. To consider how they should modify Hummer's method to suit their application, the individual researcher should consider the carbon source, pre-treatment methods, oxidizing agent and choice of protonated solvent as these can impact the C/O ratio of their final product. An overview of the popular methods can be seen in Fig. 2.

Recently, even more novel approaches to GO synthesis have been proposed. Zhang et al. synthesized larger GO sheets (108 μm average size, 256 μm at the largest) by implementing a stationary oxidation mechanism [33]. The GO obtained by typical Hummer's method is considerably smaller than its graphite source; the fractionation of GO during oxidation is due to the intense stirring during the mixing process as well as the elastic strain generated by the addition of oxygen groups to the flake surface. To create GO flakes of comparable size and morphology to the source graphite, they added H_2SO_4 and $KMnO_4$ (and subsequent H_2O_2) "without external mechanical agitations" (without stirring), thereby generating an ordered 3D structure which could then be exfoliated into ultra-large GO by "mild agitation" (manual shaking or mechanical stirring). The formation of larger GO sheets has great implications for composite materials. In another approach, Dong et al. proposed a solution to the limited dispersibility of GO in traditional solvents by creating concentrated GO slurries that can be stored and exfoliated into flakes as necessary [34]. Individual GO sheets tend to join together by π-π stacking, however ion adsorption limits GO agglomeration. By pre-oxidizing their graphite precursor and suspending in a highly-alkaline aqueous environment (pH = 14), electrostatic repulsion energy overcomes van der Waals attractive forces, so exfoliation leads to a low-viscosity slurry rather than a GO dispersion. This slurry was able to be stored at 23 wt. % solid content, and could be re-dispersed in *N*-methyl-2-pyrrolidone (NMP) or alkaline water, demonstrating a potentially critical technique for the storage and transportation of GO flakes. Both of these examples show that a deeper understanding of GO synthesis has vast implications for its scalability, properties, and applications.

2.2. Reduction of GO to rGO

In efforts to produce materials with properties as close to pristine graphene as possible, exhaustive research has been done to remove the oxygen functional groups of GO [35,36]. This reduction can be accomplished by a number of means, from thermal to chemical to electrochemical, each of which leads to differences in morphology, electrical properties, etc. The key design factors in GO reduction include the C/O ratio of the end product, selectivity in removing a single type of oxygen group (hydroxyl vs carboxylic acid vs epoxy, etc.), healing of the surface defects of the GO from oxidation, and choice of green reducing agents, as well as maintaining or improving the desired physical and chemical properties of the GO (mechanical strength, conductivity, optical properties, solubility/dispersibility of nanosheets, etc.).

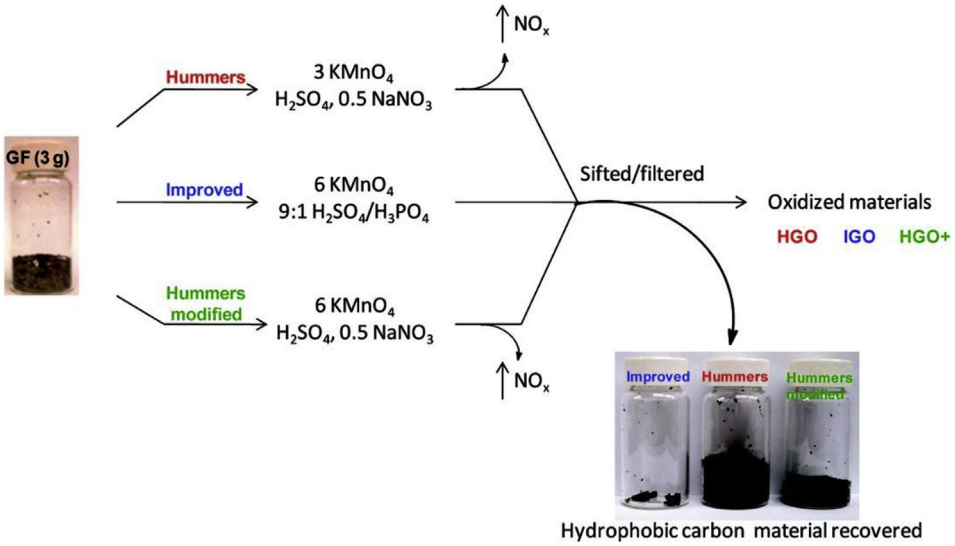

Fig. 2. Schematic of most common GO synthesis methods. Reproduced with permission from the American Chemical Society [32].

Reduction of GO by thermal treatment relies on the decomposition of oxygen groups into CO and CO_2 gases at elevated temperatures [11]. The fast evolution of these gases has also been shown to exfoliate individual GO nanosheets. A thermal reduction can be done by thermal annealing at elevated temperatures in an oxygen-free environment or by less-conventional methods such as microwaving GO powders or flash reduction of GO films by high-intensity light. The addition of chemical reducing agents to GO solutions is common and many techniques are well-supported by the literature [22], these can include hydrazine [35], metal hydrides or hydrohalic acids [11]. rGO can also be synthesized through photocatalyzed reactions. Williams et al. were able to reduce GO using UV light in the presence of a TiO2 catalyst [37]. Electrochemical reduction is also possible and doesn't require the use of chemical agents; this reduction is exclusively driven by electron exchange between GO and the electrodes of a typical electrochemical cell [38]. In recent years, a number of "green" reducing agents have been reported to be effective at synthesizing rGO, such as ascorbic acid, sugars, amino acids, and even microorganisms [36]. Different methods provide different advantages in scalability, energy usage, and amount of chemical waste produced. For further reading on the reduction of GO the authors would direct the reader to the review on the reduction of graphene oxide by Pei and Cheng et al. [39].

2.3. Graphene quantum dots (GQDs)

Recently, a new class of graphene derivatives has emerged which takes advantage of quantum confinement and edge effects of nano-scale graphene. Graphene quantum dots (GQDs) are defined as graphene nanosheets that are less than 100 nm in their lateral dimension and <10 layers (ideally one- or few-layered) of stacked graphene [40]. GQDs have been of great interest recently thanks to their stable fluorescence and adjustable band gap [13,40]. Typical production of GQDs involves further modification of GO or rGO by a number of top-down and bottom-up methods, including high-power ultrasonication, hydrothermal, solvothermal, microwave-assisted thermal treatment, and liquid-phase exfoliation [41,42]. Recently, greener alternatives have been reported, such as Lu et al. who demonstrated a 1-pot hydrothermal method which produces GQDs in only 90 min using black carbon as the source [43]. Using only hydrogen peroxide as a reagent, these GQDs were highly photo-stable and biocompatible, having great implications for bioimaging technology. Similarly, Wang et al. used a one-step, one-pot hydrothermal method to synthesize GQDs using rice husk biomass. In this case, the GQDs were tailored for Fe^{3+} sensing via luminescence quenching [44].

Detailed discussions on the synthesis routes, unique optical and electrical properties, and applications including bio-imaging, drug delivery, and photocatalysis are well covered elsewhere. The authors would refer readers to other review articles by Li et al. [40] and Tian et al. [42].

Readers should note the diversity of graphene derivatives and their many synthesis routes, and that there is no one "standard" method of obtaining GO or rGO or GQDs. However, this open-ended synthesis route allows for the implementation of many unique possibilities. These examples, as well as the others discussed throughout this review, show off the potential of GO for surface functionalization and therefore a diversity of applications for use in nanocomposite materials.

3. Properties of graphene oxide

3.1. Mechanical properties

The desirable mechanical properties of pristine monolayer graphene are well-reported; graphene is recorded as having a break strength of 42 N m^{-1}, a Young's modulus of 1.0 TPa, and an intrinsic tensile strength of 130.5 GPa [1]. The fracture toughness of graphene has also been studied by Zhang et al., and was reported to be as low as 4.0 ± 0.6 MPa $m^{1/2}$, confirming the low fracture of graphene sheets [45].

GO and rGO blends are produced in an attempt to achieve these properties, with values ranging depending on the number of surface groups and defects leftover from oxidation or other treatment processes. Suk et al. [46] reported monolayer GO (produced by a modified Hummer's method) with a Young's modulus of 207.6 ± 23.4 GPa, an order-of-magnitude drop but still notably high. Similarly, Gomez-Navarro et al. reported an rGO monolayer (produced by the original Hummer's method followed by thermal annealing in a hydrogen environment) with a Young's modulus of 250 ± 150 TPa [47].

Polymer nanocomposites benefit greatly from the use of GO and its derivatives as fillers [48]. In one example, Cheng-an et al. [49] investigated the effects of GO in polyvinyl alcohol (PVA) films produced by solution casting. They found that a 20% GO filler content was able to increase the tensile strength of the nanocomposite to 59.6 MPa, more than five times the strength of the pure PVA film. The massive improvement in mechanical properties can be attributed not only to the strength of the GO filler but the strength of the matrix/filler interface; the —OH groups of PVA and the oxygen functionalities of the GO led to a high degree of hydrogen bonding. In another, Jiang et al. [50] reported a unique combination of polyurethane (PU) with both GO and GO-reinforced carbon fibers (CF-GO) (Fig. 3A). By incorporating only 0.1 wt. % GO nanosheets into PU before molding in a vulcanizing press, the tensile strength of PU elastomer was increased from 42.4 to 49.3 MPa, a 16.4% improvement (Fig. 3B). Furthermore, by incorporating 0.1 wt. % GO as well as 1% CF-GO, the tensile strength improved to 62.1 MPa (46.4% higher). The carbon fibers had GO grafted onto their surfaces by electrophoretic deposition at 3 V of applied voltage to improve the interfacial adhesion of GO and PU. Remarkably, the elongation at break also improved for the CF-GO/PU nanocomposites thanks to the improved stress transfer from the matrix to the fillers (Fig. 3C). Bao et al. prepared rGO/polylactic acid (PLA) nanocomposites by melt blending on a twin-roller mill [51]. After preparing GO from graphite under pressurized oxidation conditions and chemically reducing it to rGO with hydrazine and ammonia, the rGO included in their nanocomposite had an average thickness of 0.4–0.6 nm and an average lateral dimension of 0.1–0.5 μm. Inclusion of these nanosheets into melt-blended PLA resulted in a storage modulus increase from 2.56 GPa to as much as 4.04 GPa at 2 wt. %.

3.2. Electrical properties

Graphene is an electrically conductive material with high electron mobility (25 $m^2 V^{-1} s^{-1}$) [52] and electrical conductivity (6500 S m^{-1}) [53] consisting of 2D layers of sp^2 carbon one atom thick. Graphene has been shown to greatly improve the electrical conductivity of polymers at low filler contents (e.g., 0.1 S m^{-1} at 1 vol% in polystyrene(PS)) [54]. In the general fabrication of GO, the process results in disruption of the sp^2 bonding orbitals of graphene and the addition of abundant surface groups that inhibit its electrical conductivity, making GO electrically resistive (1.64×10^4 Ω m) [55,56]. As a result of this high resistivity, researchers have explored reduction techniques of GO to form rGO. Upon reduction, the electrical conductivity of GO can be greatly improved and can be tuned over several orders of magnitude with conductivities ranging from (~0.1 S m^{-1}) [57] to (2.98×10^4 S m^{-1}) [58]. Even after reduction, the rGO contains residual sp^3 bonded carbon to oxygen, which disturbs the movement of charge carriers through the rest of the sp^2 clusters. Electrical transport in rGO occurs primarily by hopping, which differs from that of mechanically exfoliated graphene [59].

Based on this necessity to reduce GO, researchers have been exploring various techniques to improve the synthesis of electrically conductive rGO. For example, Stankovich et al. [60] reduced a colloidal suspension of GO exfoliated in water with hydrazine hydrate, which exhibited an electrical conductivity of 2×10^2 S m^{-1}, improving the conductivity of the GO by 5 orders of magnitude. Voiry et al. [61] used a conventional microwave at 1000 W for 1–2 s to form rGO which improved the electron mobility of GO from ca. 1×10^{-4} to over 0.1 $m^2 V^{-1} s^{-1}$ in field effect

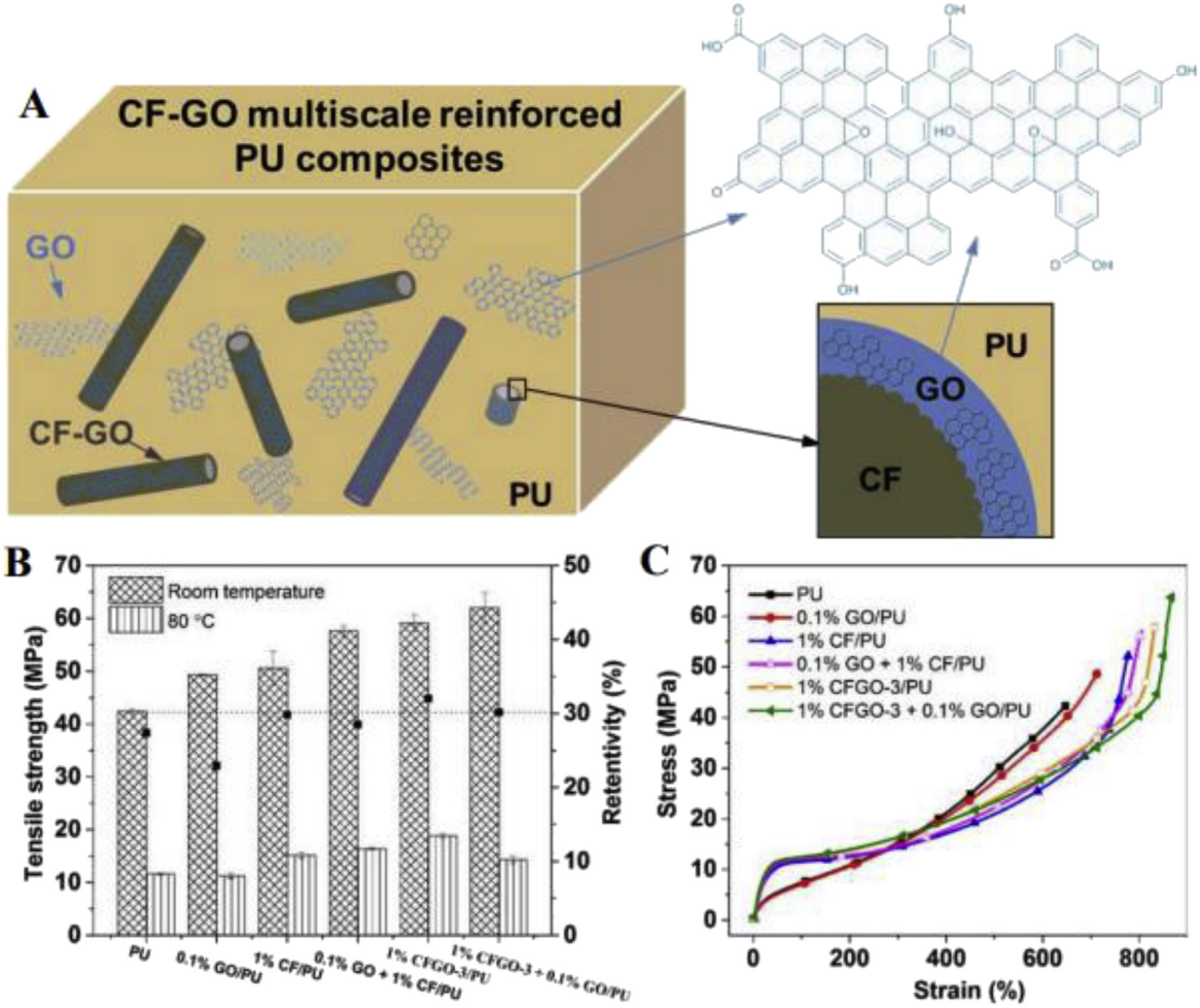

Fig. 3. (A) Schematic illustration of the CF-GO multiscale reinforcements for PU elastomer nanocomposites. (B) Tensile strength of PU-based materials at room temperature and its retentivity at 80 °C. (C) Stress-strain curves of PU-based materials. Reproduced with permission from the Society of Plastics Engineers [50].

transistors. Other methods have also been shown effective in synthesizing highly conductive rGO, including immersion in hydroiodic acid [62,63] and activation with KOH [64].

The enhanced electrical properties of rGO have made it a promising material as a conductive filler to add to polymer matrices for uses in a wide array of materials. For example, Kim et al. [65] developed a highly flexible supercapacitor of polyaniline (PANI) with rGO with a capacitance of 431 $F\,g^{-1}$. This material had a maximum electrical conductivity at a 24 wt. % rGO of $9.06 \times 10^4\,S\,m^{-1}$, which improved upon the individual components which had electrical conductivities of $5.80 \times 10^4\,S\,m^{-1}$ and $4.65 \times 10^3\,S\,m^{-1}$ for PANI and rGO, respectively. The improved performance was a result of forming a more compact packing of the PANI chains by inducing an expanded conformation of the PANI chains with π- π interactions between rGO and PANI. Hou et al. [66] developed an rGO/cellulose nanofiber(CNF) paper with an electrical conductivity of $4.38 \times 10^3\,S\,m^{-1}$ using a novel sandwich structure of CNF covered on top and bottom with rGO. The composite only contains 4 wt. % rGO and showed superior conductivity over blending of the rGO in CNF. Wan et al. [67] developed a conductive artificial nacre by mixing GO with chitosan (CS) in a three-step process. First, a GO solution was mixed with CS to coat the GO with CS. In step 2, the authors used vacuum filtration to assemble a nanocomposite film. The final step was to reduce the GO with hydroiodic acid to form an rGO/CS nanocomposite with the highest electrical conductivity of $1.553 \times 10^4\,S\,m^{-1}$ at 95 wt. % rGO, which was lower than the pure rGO, but which saw improvements to both tensile strength and toughness. In addition to the polymers mentioned above, rGO has also been added to numerous other polymers to improve their electrical properties including polyethylene terephthalate (PET) [68], polydimethylsiloxane (PDMS) [69], PVA [70], and PU [71].

3.3. Thermal properties

Like its electrical conductivity, synthesized GO from graphite has a low thermal conductivity of 0.5–1 $W\,m^{-1}\,K^{-1}$ making it not an ideal option for most applications requiring good thermal properties [72]. Graphene, on the other hand, has been shown to have one of the highest in-plane thermal conductivities of known materials, with a thermal conductivity of ~3000–5000 $W\,m^{-1}\,K^{-1}$ [8,54]. As a result, reduction of GO is critical for incorporation of rGO into polymers to improve their thermal conductivity [73]. Renteria et al. [72] showed that producing rGO films by annealing GO at high temperature (1000 °C) can significantly improve the in-plane thermal conductivity, showing an improvement from ~3 to 61 $W\,m^{-1}\,K^{-1}$. The films showed an interesting anisotropy in terms of thermal conductivity as the cross-plane thermal conductivity decreased to ~0.09 $W\,m^{-1}\,K^{-1}$ and showed a ratio of the two (in-plane/cross-plane thermal conductivity) of 675. This may prove useful for certain applications where directional heat conduction is important.

The incorporation of rGO into polymers has led to profound

improvements in the thermal conductivity of the resultant nanocomposites. Kumar et al. combined rGO with poly(vinylidene fluoride-co-hexafluoropropylene). At 27.2 wt. % rGO, the nanocomposite showed a thermal conductivity of 19.5 $W m^{-1} K^{-1}$, which was a significant improvement over the neat polymer and larger than many common alloys. The enhanced thermal conductivity was believed to be a result of the high conductivity of the rGO, which was able to provide a path of lower thermal resistance for traveling phonons, thanks to the large aspect ratio and the interfacial contact area of the rGO. Other important factors to improved thermal conductivity would be for high orientation of the rGO sheets and large sheet size that limits the thermal transfer along boundaries. rGO has also been shown to improve the thermal properties of many other polymer systems including, epoxy [74,75], PVA [76,77], and styrene butadiene rubber [78].

While for many applications it is useful to have a high thermal conductivity, it is not the case for all situations. In some instances, it is useful to provide high thermal insulation properties such as in-home insulation and in flame retardants. GO has recently been shown to be an effective filler to improve the flame retardant properties of various polymer nanocomposites [79–83]. For example, Wicklein et al. [84] added GO and sepiolite clay nanorods (SEP) to CNF to develop a super-insulating flame retardant foam, which could find applications as an insulating material. The films had a thermal conductivity of 15 $mW m^{-1} K^{-1}$ which is below that of common insulation materials, such as expanded PS, PU, and mineral wool that have thermal conductivities of ~35, 25, and 35 $mW m^{-1} K^{-1}$, respectively. The porous foams were made by freeze casting colloidal suspensions of the three materials. Fig. 4A presents the SEM cross-section of the nanocomposite foam, showing highly aligned tubular pores with a diameter of ~20 μm and a wall thickness of ~0.3 μm. When subjected to a vertical flame test the foam stopped the flame from self-propagating and showed a 25% lower peak heat release rate (pkHRR) than a foam of just CNF alone (Fig. 4B and C). This result shows the substantial ability of GO nanofillers to imbue important thermal properties in non-traditional systems.

4. Applications of GO and rGO

4.1. Membranes and coatings

4.1.1. Gas transport

Owing to GO's negatively-charged surface and large aspect ratio nanosheet structure giving exceptional impermeability to most gases, GO-based membranes have found wide application in gas barrier nanocomposites [85,86]. Numerous reviews on polymer nanocomposites exist which compile many instances of barrier property improvements by graphene derivatives as fillers [3,12,14,87]. As in the rest of research done in the field of high-gas-barrier properties of polymer nanocomposites [88–91], it is generally regarded that 2D fillers can be oriented in a polymer matrix to create a "tortuous" path for gas molecules (Fig. 5A). This involves GO and rGO nanosheets aligned in a nacre-like structure, taking advantage of the fillers' high aspect ratio and surface functionalization by oxygen groups.

In a typical example, Kausar was able to produce rGO/polyamide nanocomposite films which showed great improvements in barrier properties [94]. Their GO was produced by a modified Hummer's method and subsequently reduced to rGO using hydrazine hydrate in an aqueous solution. Polyamide 1010 (PA1010) and fluorinated polyamide (FPA) were refluxed in an 80/20 blend in an *N*-methyl-2-pyrrolidone (NMP) solvent for 24 h. The desired amount of rGO was added and refluxed for an additional 2 h before solution-casting onto a glass substrate. After removal from the glass, the free-standing films showed increased barrier properties, as well as enhanced mechanical strength, thermal stability, flame resistance, and adhesive strength. In particular, the films with only 3% rGO loading showed a 47% reduction in oxygen permeability and a 21% reduction in water vapor permeability over the 80/20 polyamide blend alone. This is attributable to the high vapor barrier of rGO and the increased path tortuosity of the gas molecules. This finding is of particular interest for engineering applications, as polyamides are a common engineering plastic but face the issue of high air permeability and moisture absorption.

Similarly, Pierleoni et al. fabricated GO/polyethyleneimine (PEI) nanocomposites to form a high oxygen barrier and fine-tune the film properties to generate a selective gas barrier [95]. Using layer-by-layer deposition, they were able to fabricate tunable coatings on two common substrates, PET and Matrimid (a commercial gas membrane). Using GO nanosheets with a 25 μm average lateral dimension, each GO/PEI bilayer had a 3.7 nm sheet spacing demonstrating a closely-packed and well-oriented nanosheet structure. The result of this was a coated PET film showed a 96% reduction in oxygen transmission rate.

Liu was able to fabricate two different GO/PVA nanocomposite coatings using a scalable one-step dip-coating method [93]. Using an aqueous suspension of PVA and GO nanosheets with an average lateral dimension of ca. 3.5 and 0.53 μm, Liu was able to align the GO nanosheets using gravity-assisted orientation. This led to a 99.1% reduction in oxygen transmission rate (OTR) compared to the PET substrate with only 10 vol. % of the 3.5 μm GO nanosheets, showing comparable performance to inorganic montmorillonite (MMT) clay nanosheets. The smaller GO nanosheets also showed significant improvement to the OTR of the coated PET film, but remained higher at all concentrations compared to the larger nanosheet size. The small GO also exhibited a slight increase in OTR when increased from 10 to 30 vol. %, which is believed to be due to the increase in viscosity of the coating solution that partially disrupted the orientation of the small GO nanosheets (Fig. 5B). It is believed that the exceptional improvement to the barrier properties is owing to the

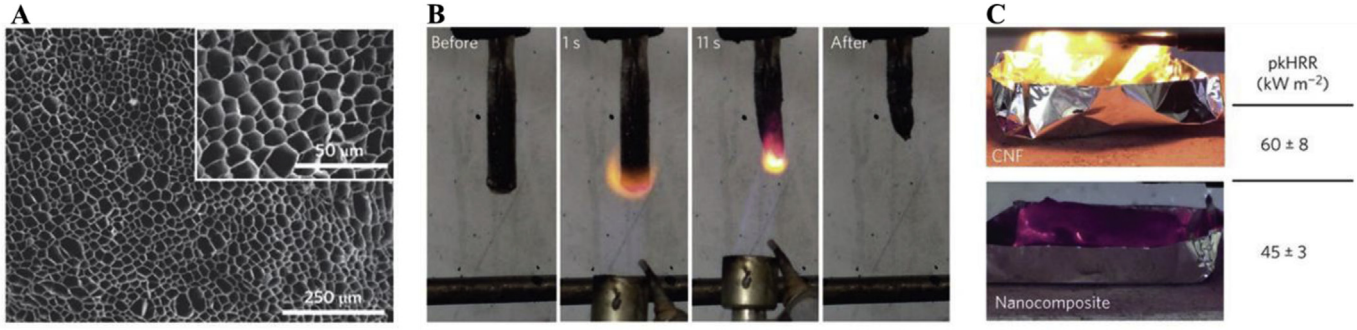

Fig. 4. (A) SEM cross-section image of a freeze-cast nanocomposite foam containing CNF, GO, SEP and boric acid (BA). (B) Vertical burn test (UL94) of a nanocomposite foam containing 77 wt. % CNF, 10 wt. % GO, 10 wt. % SEP and 3 wt. % BA. The panel shows the foam before the test, after 1 and 11 s of application of a methane flame, and the foam after the test, showing high fire retardancy. (C) Photographs of CNF and CNF/GO/BA/SEP nanocomposite foams during the cone calorimetry test with the corresponding pkHRR. The test reveals high combustion resistance for the nanocomposite foam at the limit of non-ignitability, while CNF foams are entirely combusted. Reproduced by permissions of Springer [84].

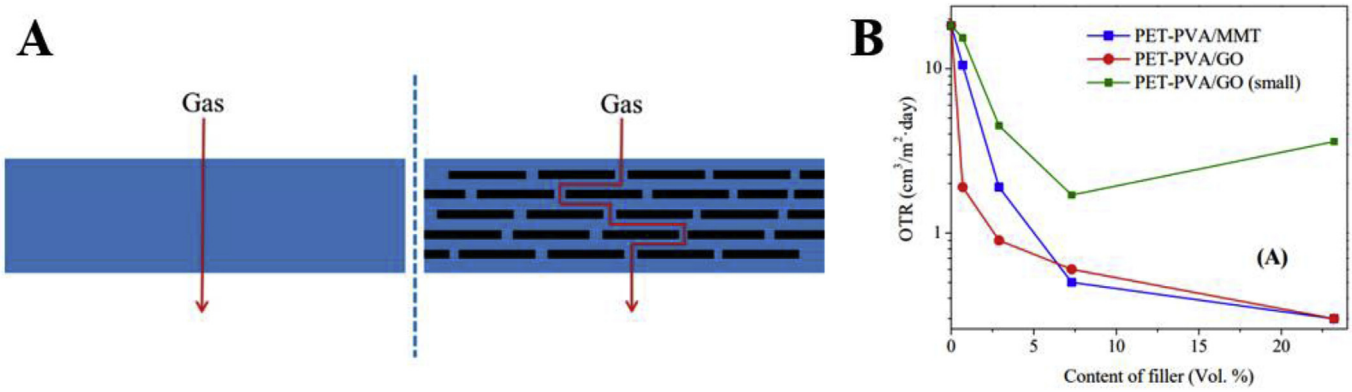

Fig. 5. (A) Comparison of gas molecule passing through a neat polymer film (left) and a polymer film containing a high concentration of well-aligned impermeable nanosheets (right). Reproduced with permission from the American Chemical Society [92]. (B) OTR of GO/PVA-coated PET films as a function of nanosheet concentration. The red line ("PVA/GO") represents GO filler with a lateral sheet dimension of 3.5 μm, while the green line ("PVA/GO (small)") represents a lateral dimension of 0.53 μm. Reproduced from permission from the University of Connecticut [93]. (For interpretation of the references to color in this figure legend, the reader is referred to the Web version of this article.)

high level of alignment of the GO nanosheets, which can be well oriented via gravity assisted flow of a thin liquid layer [96].

Due to its exceptional ability to form high barrier films to most small molecular weight species, GO is often not considered for gas separation processes. However, in recent work researchers were able to demonstrate the remarkable ability of GO-based membranes to generate atomically-thin highly selective gas transport membranes with selective structural defects to allow for the transport of small molecules. Li et al. [97] developed GO membranes with thicknesses as thin as 1.8 nm through a facile vacuum filtration process. It was found that hydrogen permeated 300 times faster than CO_2 (or N_2) with mixture separation selectivities of 3400 for H_2/CO_2 and 900 for H_2/N_2. Shen et al. [98] developed 2D GO channels for super-fast gas separation by controlling the outer external forces (compressive, centrifugal, and shear forces) and the inner external forces (molecular interactions) to control the GO nanostructure through a vacuum-spin technique to fabricate the membranes. By coupling the GO nanosheets with PEI they were able to control the electrostatic interaction, covalent binding, and hydrogen bonding between the GO

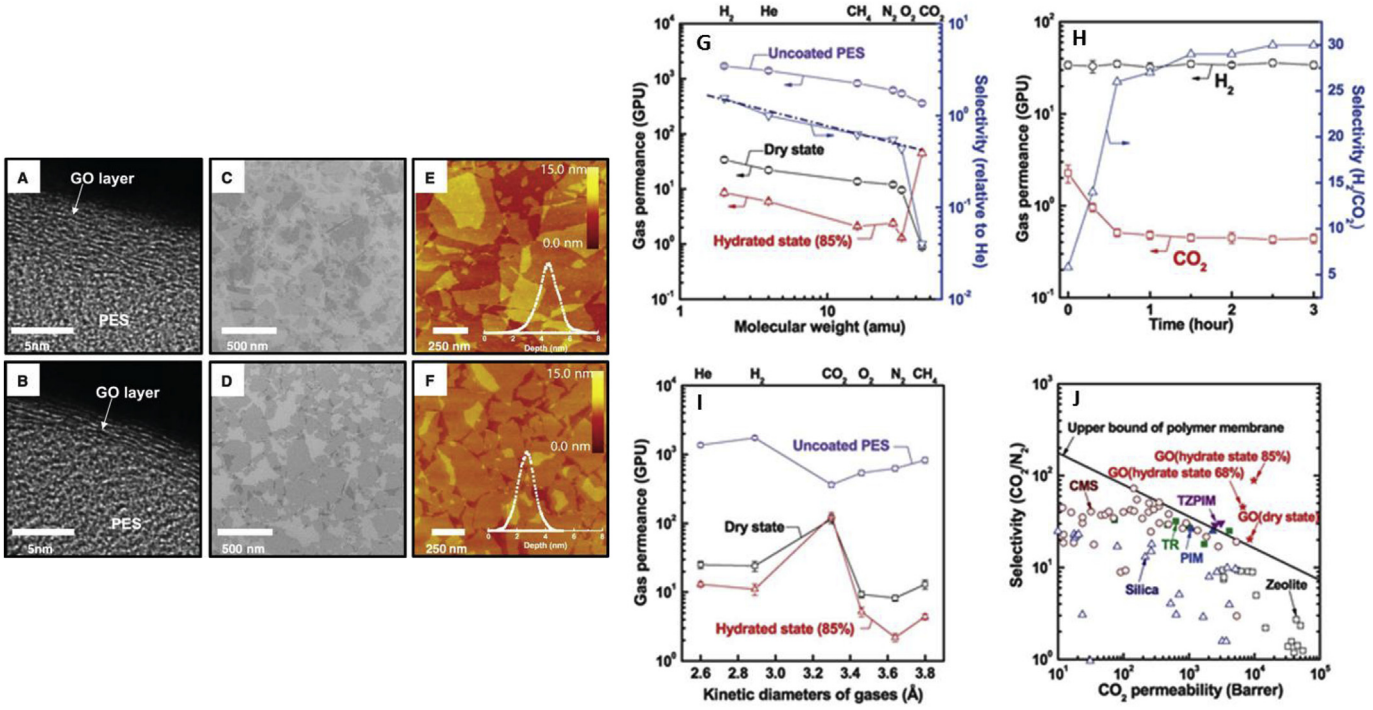

Fig. 6. TEM images of ultrathin GO membranes cross-sections of (A) method 1 and (B) method 2; SEM images of GO films coated on a wafer via (C) method 1 and (D) method 2; AFM images of GO membrane surfaces; the inserts show depth profiles of GO membrane surfaces. (E) Method 1 [root mean square roughness (Rq) = 0.8 nm, average roughness (Ra) = 0.614 nm]; (F) method two (Rq = 0.608 nm, Ra = 0.467 nm); (G) Gas permeances of GO membranes as a function of molecular weight (method 1; dashed line represents the ideal Knudsen selectivity) under dry and humidified conditions. amu, atomic mass unit; (H) H_2 and CO_2 permeances and H_2/CO_2 selectivity of method 1 GO membranes as a function of permeation time; (I) Gas permeances of GO membranes as a function of kinetic diameter (method 2) under dry and humidified conditions; (J) Relation between CO_2 permeability and CO_2/N_2 selectivity of method 2 GO membranes under dry and humidified conditions with other literature membranes [thermally rearranged(TR) [100]; tetrazole(TZ) polymers of intrinsic micro-porosity(PIM) (TZPIM) and PIM [101]; Carbon Molecular Sieve membranes (CMS) [102]]. Error bars indicate the standard deviation of all raw data. Reproduced by permissions of the American Association for the Advancement of Science [99].

nanosheets and the PEI. The 2D channels had interlayer heights of ~0.4 nm allowing for fast but highly selective gas sieving, with an H_2 permeability of 840–1200 Barrer and an H_2/CO_2 selectivity of 29–33.

By controlling the stacking of GO nanosheets through irregular layered stacking, Kim et al. [99] were able to design gas separation membranes for highly selective gas diffusion. By preparing ultrathin GO membranes on a polyethersulfone (PES) support via two different coating methods, with thicknesses ranging from ~3 to 10 nm (Fig. 6A and B), the authors were able to control the flow of gases through the channels and pores of the GO film to generate highly selective membranes. In method 1, layers of GO were coated on the PES by putting the PES surface in contact with a GO solution at the liquid-air interface followed by spin-coating. This method enabled the coating to be influenced by the electrostatic and hydrophilic interactions of the GO nanosheets with the PES support. Edges of GO sheets are negatively charged, so edge-to-edge repulsion led the GO nanosheets to assemble into a heterogeneous island-like structure on the membrane surface (Fig. 6C and E). In method 2, the GO membranes were prepared by spin-coating the GO solution directly on the PES surface, leading to a denser stacking of the GO sheets from the capillary interactions between the GO sheet faces (Fig. 6D and F). TEM images of the cross-sections of the GO membranes show the different stacking structures of each coating method (Fig. 6A and B). The membranes prepared by method 1 show behaviors that can be explained by Knudsen diffusion of gases in nonporous membranes with gas permeance decreasing with increases in molecular weight of the gases. But this did not hold true for CO_2 (Fig. 6G), which showed a sharp decrease in gas permeance as compared to other gases. Within the first hour of the permeance test, CO_2 permeance decreased quickly before leveling out (Fig. 6H), while other gases did not show this drastic reduction in permeance. Using method 1 a high H_2/CO_2 selectivity of 30 was achieved. With method 2, an interlocked layer structure was generated showing very different behaviors to method 1 with CO_2 showing the highest permeance in both dry and hydrated states (Fig. 6I). Under hydrated conditions, the permeability of all gases decreased except for CO_2, leading to highly selective diffusion between the GO interlayers generated via this method at high humidity, showing higher CO_2/N_2 selectivity than other reported polymer membranes (Fig. 6J).

4.1.2. Water treatment

GO membranes are widely considered promising materials for water treatment application because of their high water permeance [103–105] and stability in water [106]. As a result, significant progress has been made during the past few years in developing high permeance membranes while maintaining high rejection rates. For example, Thebo et al. [107] fabricated GO sheets on polydopamine modified PES supports with tannic acid and theanine amino acid as crosslinking agents. These membranes demonstrated water permeance over 10,000 L m^{-2} h^{-1} bar^{-1} with dye rejection of ~100% for rhodamine B and methylene blue. Bano et al. [108] developed a GO/polyamide nanocomposite which showed a 12 fold increase in water flux over the base polyamide membrane while maintaining high salt rejection with the incorporation of 0.2 wt. % GO in the polyamide by improving the hydrophilicity of the nanocomposite membrane.

Typically, GO membranes have difficulty in certain aspects of water treatment, such as desalination. The interlayer spacing of GO can swell from 7.76 to 17.63 Å in dry and hydrated conditions, respectively [106]. As such, the diameters of hydrated ions of common salts are smaller than this hydrated value leading to poor salt rejection by the GO membranes [109]. Abraham et al. [110] was able to develop a GO membrane that maintains a lower interlayer distance through physical confinement (Fig. 7A–D) of the GO nanosheets by embedding them in epoxy, maintaining an interlayer spacing of 9.8–6.4 Å at varying relative humilities (Fig. 7E). As a result of this controlled spacing, the permeation rates through the membrane of controlled interlayer distances showed exceptionally low permeation for the salts used (Fig. 7F). With lower interlayer distances the permeation clearly decreases and with an interlayer spacing of ~6.4 Å there was no detectable ion concentration in the permeate. The above results show that through precise control of the

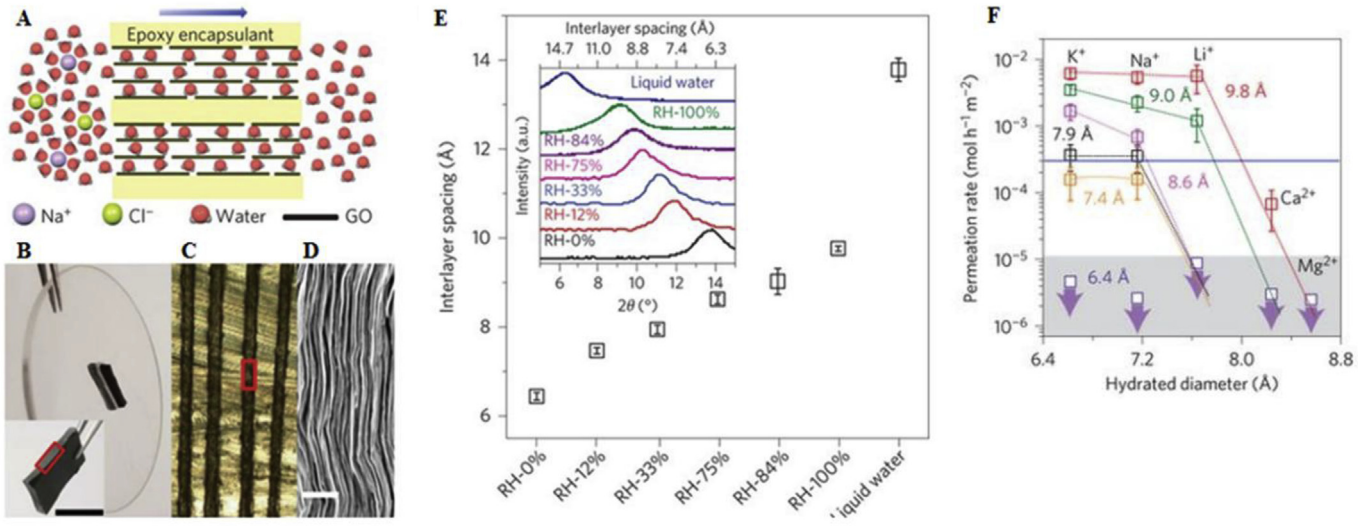

Fig. 7. (A) Schematic illustrating the direction of ion/water permeation along graphene planes. (B) Photograph of a physically confined GO (PCGO) membrane glued into a rectangular slot within a plastic disk of 5 cm in diameter. Inset: photo of the PCGO stack before it was placed inside the slot. Scale bar, 5 mm. (C) Optical micrograph of the cross-sectional area marked by a red rectangle in B, which shows 100 μm-thick GO laminates (black) embedded in epoxy. Epoxy is seen in light yellow with dark streaks because of surface scratches. (D) Scanning electron microscopy image from the marked region in C. Scale bar, 1 μm. (E) Humidity-dependent interlayer spacing found using X-ray diffraction (inset). The case of liquid water is also shown. Error bars denote standard deviations using at least two measurements from three different samples. (F) Permeation rates through PCGO membranes with different interlayer distances (color-coded). The salts used were KCl, NaCl, LiCl, $CaCl_2$, and $MgCl_2$. The hydrated diameters are taken from the literature [109]. Dashed lines are guides to the eye indicating a rapid cutoff in salt permeation, which is dependent on the interlayer spacing. Grey area shows the below-detection limit for our measurements lasting five days, with arrows indicating the limits for individual salts. The horizontal blue line indicates our detection limit for Cl^-. Both cations and anions permeated in stoichiometric quantities were found above the latter limit. Error bars denote standard deviation. Reproduced by permissions of Springer [110]. (For interpretation of the references to color in this figure legend, the reader is referred to the Web version of this article.)

interlayer distance of the GO nanosheets exceptional salt rejection can be maintained.

The use of GQDs has also been reported in membrane technology thanks to their high dispersibility in water, high specific surface area, hydrophilicity, and antifouling performance [111–113]. Zhang et al. developed a nanofiltration membrane by incorporating GQDs synthesized by bottom-up pyrolysis of citric acid into a tannic acid (TA) aqueous dispersion [114]. Polyacrylonitrile (PAN) membranes were submerged in this dispersion for 20 min, then submerged into isophorone diisocyanate in *n*-hexane to polymerize the TA. At 0.5 g L^{-1} GQD content, the resulting GQD/TA membranes showed a water flux of 23.33 L m^{-2} hr^{-1} and a high rejection of Congo red (99.8%) and methyl blue (97.6%) while operating at a low 0.2 MPa. Furthermore, with an increasing filler content the membranes had lower ζ-potential (−8.37 mV at 0.25 g L^{-1}, -18.2 mV at 1 g L^{-1}) thanks to the carboxyl groups on the edges of the GQD nanosheets, as well as an increased resistance to fouling (a total flux decline rate of 55.1% for plain TA membranes and 21.6% for 1 g L^{-1} GQDs) thanks to the hydrophilic nature of GQDs.

4.2. Stimuli-responsive materials

4.2.1. Humidity actuation

As is well discussed, GO films have a strong affinity for water whereupon the oriented GO nanosheets swell as water enters between them. In addition, GO/polymer nanocomposites have improved mechanical properties, providing structural stability in humid environments. For sufficiently thick hydrophilic films exposed to water, there results an asymmetric swelling causing bending of films that results in reversible actuation of polymer films upon hydration/dehydration cycling [115–117]. Zhang et al. [118] demonstrated a biomimetic film actuator by combining GO with CS, a hydrophilic polymer, to form a nacre-like structure that shows continuous flipping when exposed to humidity from one side. Even though CS is hydrophilic, a film on its own has insufficient mechanical properties to demonstrate any actuation performance. When combined with GO, the Young's modulus of the resultant nanocomposite reaches 2.4 GPa and exhibits a tensile strength of 66.5 MPa which respectively are 3.2 and 2.0 times that of dry CS alone. This is a significant improvement to the mechanical properties which allows for the film to continuously flip over if exposed to water from one side. Since diffusion of water is dependent upon film thickness and temperature, it is not surprising that there is increased flipping frequency with thinner films and higher temperature (Fig. 8A and B). When thin strips of the CS and GO/CS films are exposed to humidity there is a clear difference in bending angle (Fig. 8C). In addition, the GO/CS film is able to lift 10 times its own weight and achieve the same bending angles as with no cargo with a work output of 6.17 J kg^{-1} and a power density of 0.39 w kg^{-1} (Fig. 8D and E). Even with an increased cargo weight, the film is still able to maintain a flipping frequency of 4 (Fig. 8F). The results show that there is potential for these GO/CS films to turn humidity induced actuation into usable mechanical work.

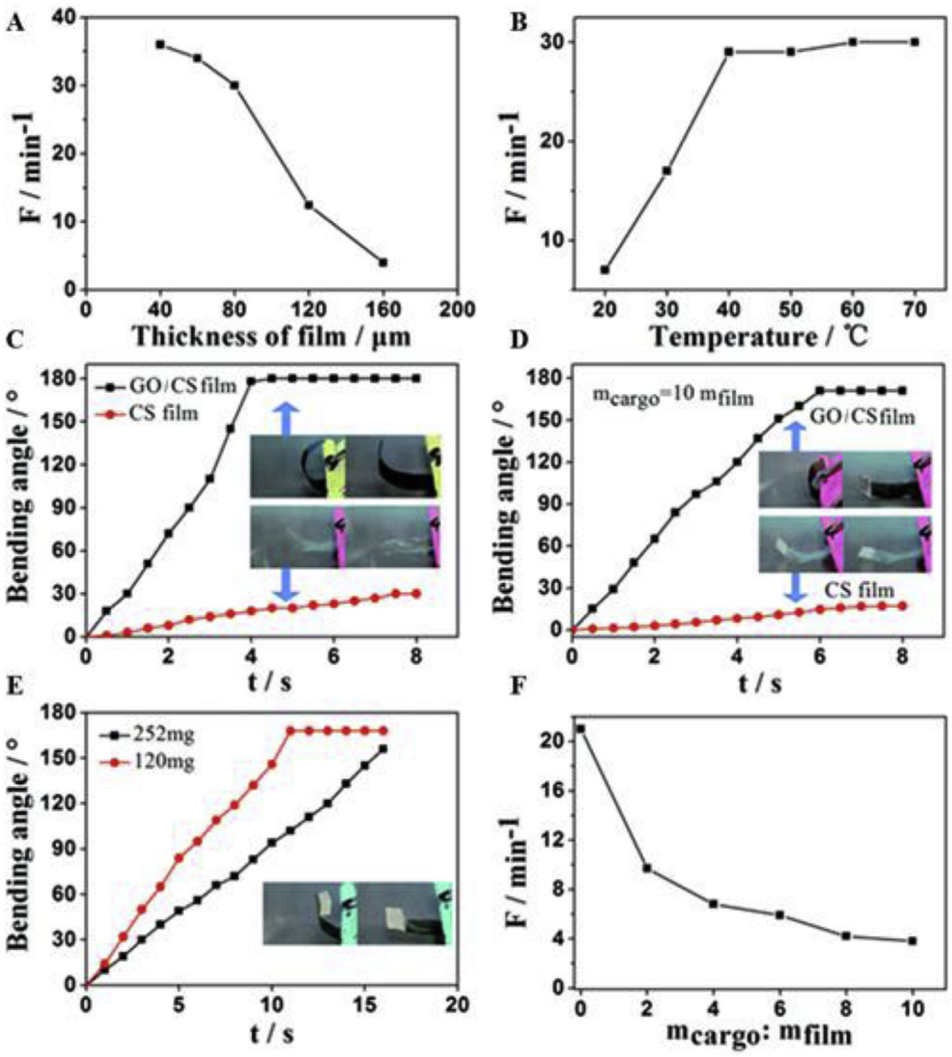

Fig. 8. Effects of (A) film thickness (water temperature: 40 °C) and (B) temperature (film thickness: 60 mm) on the flipping frequency F. (C) Performance of the GO/CS nanocomposite film and pure CS in hygro-induced bending. Film dimensions: 2 cm × 0.5 cm × 0.040 mm; film weight: 6 mg for nanocomposite, 5 mg for pure CS; water temperature: 37 °C (D) Humidity-induced bending of the hybrid film and pure CS loaded with a cargo 10 times heavier than themselves. The shapes of the hybrid film and water temperature are the same as C. (E) Effect of the cargo weight on humidity-induced bending. Film size: 1.4 cm × 0.5 cm × 0.037 mm; film weight: 37 mg; cargo weight: 252 mg and 120 mg; water temperature: 37 °C. (F) Flipping frequency of the hybrid film as a function of the cargo-to-film weight ratio. Film size: 2 cm × 2 cm × 0.043 mm; film weight: 15 mg; water temperature: 37 °C. Reproduced by permissions of the Royal Society of Chemistry [118].

4.2.2. Thermal/light responsive actuation

As is well documented, GO is efficient in photothermal conversion of light in nanocomposites [119–122]. As such, it has proven an excellent filler to add to polymer nanocomposites to develop actuators that respond to heat and near-infrared light (NIR) [123,124]. For example, Kim et at [125]. developed a thermally responsive GO fiber that showed torsional and tensile actuation upon heating. The GO was mixed with a nylon-6,6 polymer by wet spinning and showed two different types of actuation depending upon the fabrication of the fiber which could be twisted and wound to form coils with a homochiral structure or heterochiral structure. The fibers undergo volume expansion upon heating showing 80% contraction for the homochiral direction and heterochiral elongation of 75%. The fibers are capable of lifting 100 times their own mass and can even withstand temperatures above the melting temperature of the nylon.

In another report, Zhao et al. [126] designed multiple bionic hydrogel actuators with GO and *N*-isopropylacrylamide and 4-hydroxybutyl acrylate as a monomer and crosslinking agent, respectively. Two methods were used to infiltrate the GO into the hydrogel; one was to fully immerse the hydrogel in GO aqueous solution to allow for complete infiltration and the other was to use local infiltration of the GO by selectively applying a GO solution to specific areas of the dried hydrogel. The authors were able to design a NIR-driven bionic chrysanthemum via the entire infiltration as seen in Fig. 9A. This bionic chrysanthemum responded to NIR light and exhibited a closing state under illumination and an open state in the dark (Fig. 9A(a-f)). For the second method of local infiltration, the authors designed a bionic hand that would locally deform in response to NIR light (Fig. 9B). The hand could show selective bending of individual fingers in response to applied NIR light and would return to the open state in the dark (Fig. 9B(a-i)), showing the potential for GO-based actuators to be used as touchless sensors and in soft robotic applications.

4.2.3. Electromechanical actuation

As well discussed, rGO shows exceptional electrical conduction properties when encapsulated in polymer matrices. So, it is no surprise that this endows rGO/polymer nanocomposites with excellent electrical stimuli-responsive actuation [127–131]. In the paper by Kim [132], the authors were able to develop a durable and water-floatable electromechanical actuator utilizing rGO as the electrode for the material. In most traditional ionic polymer-metal composite (IPMC) actuators there are persistent problems under extended excitations in air, as cracks form in the surface allowing for leaching of the electrolyte as demonstrated in Fig. 10A. To solve this problem the authors combined rGO with the polymer Nafion-117 and the ionic liquid xxx-BF_4 to alleviate the development of cracks in the actuator to form an ionic polymer graphene composite actuator (IPGC). But upon the introduction of rGO, there becomes a problem of poor adhesion with the ionic polymer. The authors found a unique way of solving this problem by using an asymmetrically-modified rGO paper with a smooth outer surface that is hydrophobic and a rough inner surface by laser-scribing the rGO surface as shown in Fig. 10B. This allowed the IPGC to withstand repeated bending tests and maintain a water contact angle of 86°, allowing for the actuator to float on the water surface. The IPGC exhibited controlled responses to four different driving voltages from 2 to 5 V at an excitation frequency of 0.01 Hz as seen in Fig. 10C and D. As the voltage is increased, there is a corresponding increase in tip displacement with the largest being 4.26 mm at a voltage of 5 and control over direction with positive or negative applied voltage.

4.2.4. Multi-stimuli actuation

With the diverse properties of GO/rGO showing excellent application in various stimuli-responsive actuation materials, it is then desirable to explore the different combinations of the actuating stimuli. For example, Chen et al. [133] developed a multi-responsive actuator responding to both humidity and NIR by making a nanocomposite of GO and biaxially oriented polypropylene (BOPP). For this nanocomposite, the GO layer is very hygroscopic and thus highly sensitive to ambient humidity, while the BOPP is inert to humidity. This provided the GO/BOPP film with excellent humidity-driven actuation based on the large asymmetric swelling generated from the two layers. The film fabricated in 50% relative humidity (RH) rested in a flat state, but when the RH humidity was reduced to 20% with dry air, the film bent to the GO side with a curvature of 2.5 cm^{-1} as the interlayer distance of the GO nanosheets decreased due to the loss of water. The film returned to its initial flat state when rehydrated at 50% RH. At higher RH (65%), the film would bend to the BOPP side as the GO film swelled, resulting in a curvature of 3.1 cm^{-1} due to the swelling of the GO sheets. In addition to the humidity response, this GO/BOPP actuator also responded to NIR light, converting the light energy into thermal energy through a photothermal effect as GO

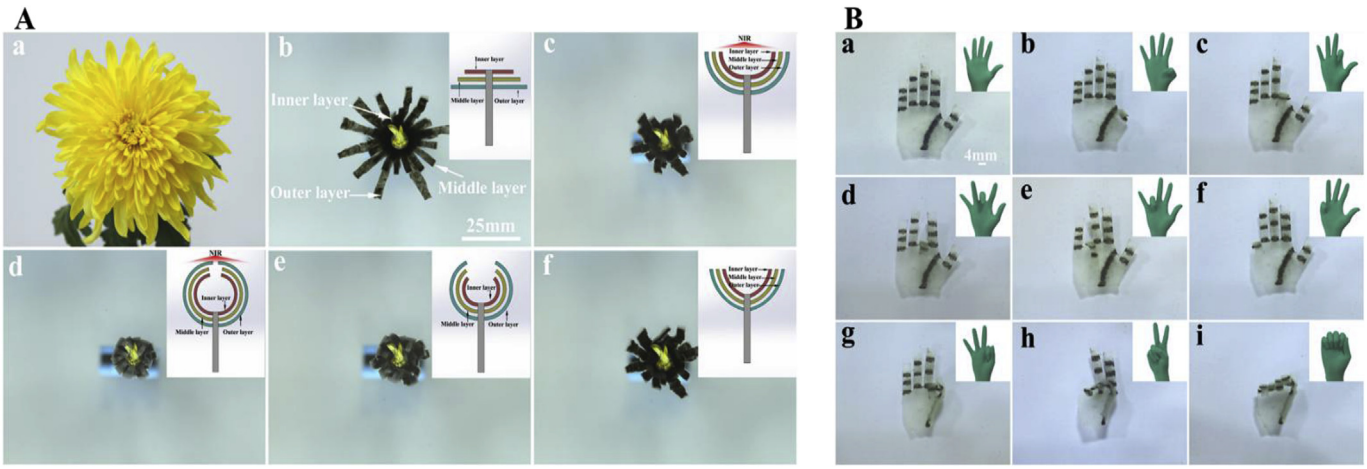

Fig. 9. (A) Deformation process of a NIR-driven bionic chrysanthemum fabricated via entirety infiltration. The bionic chrysanthemum was composed of three H-1 layers. Under NIR stimulation, the bionic chrysanthemum changed from the closed state to the open state. (a) Image of a real chrysanthemum; (b) initial state of the bionic chrysanthemum; (c) closing state of the bionic chrysanthemum; (d) closed bionic chrysanthemum; (e) opening state of the bionic chrysanthemum; (f) opened bionic chrysanthemum. (B) Deformations of a NIR-driven bionic human hand fabricated via locality infiltration. Inspired by the human hand, the locality infiltration of GO was used to imitate the spacing of joints in a real hand. (a) Initial state of the bionic hand; (b) deformation of the thumb; (c) deformation of the index finger; (d) deformation of the middle finger; (e) deformation of the ring finger; (f) deformation of the little finger; (g) gesture of "OK"; (h) gesture of "victory"; (i) gesture of "fist". Reproduced with permissions from Elsevier [126].

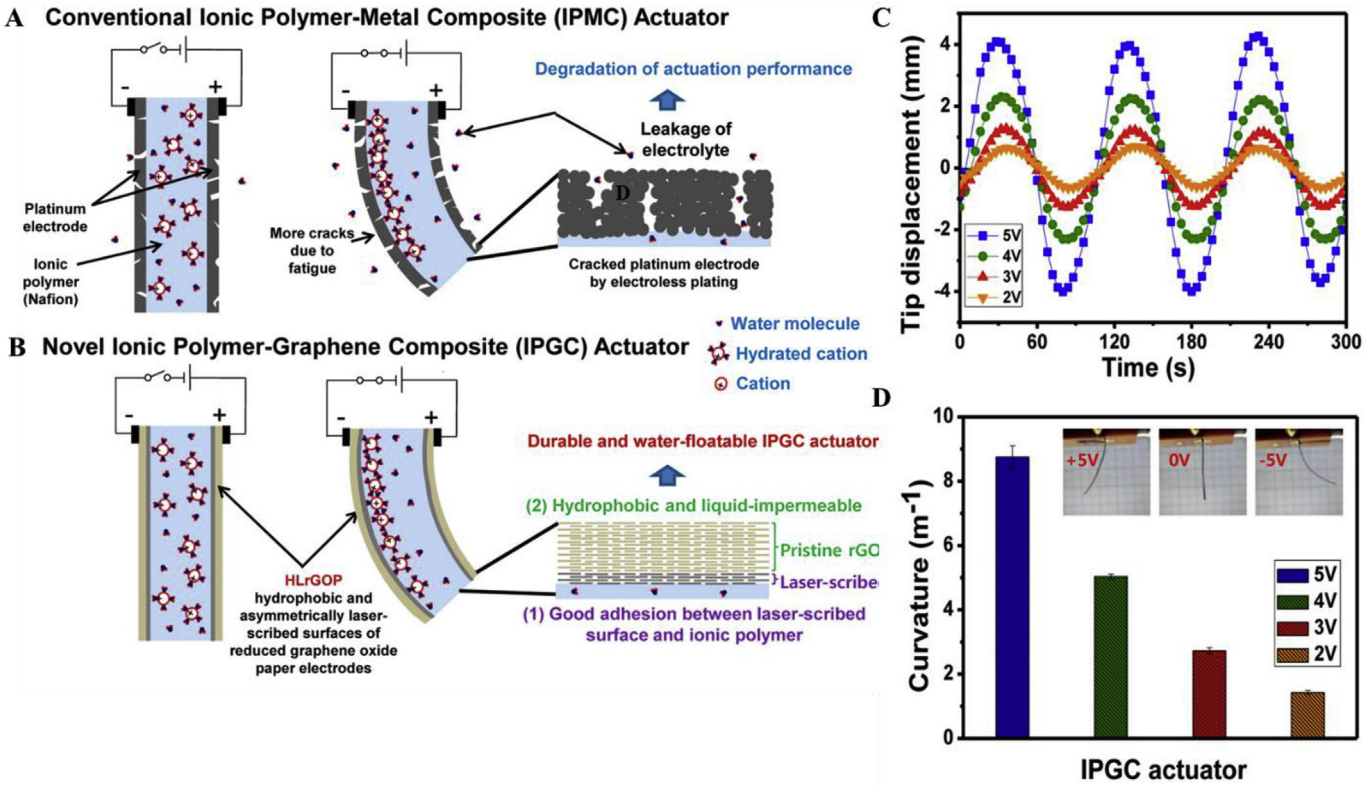

Fig. 10. Schematic representations of the structures and mechanisms of (A) liquid-permeable IPMC actuator and (B) durable and water-floatable IPGC actuator. Bending actuation performances of IPGC actuators with EMIBF4 electrolyte (C) under various input voltages and (D) their corresponding curvatures. Reproduced by permissions of the American Chemical Society [132].

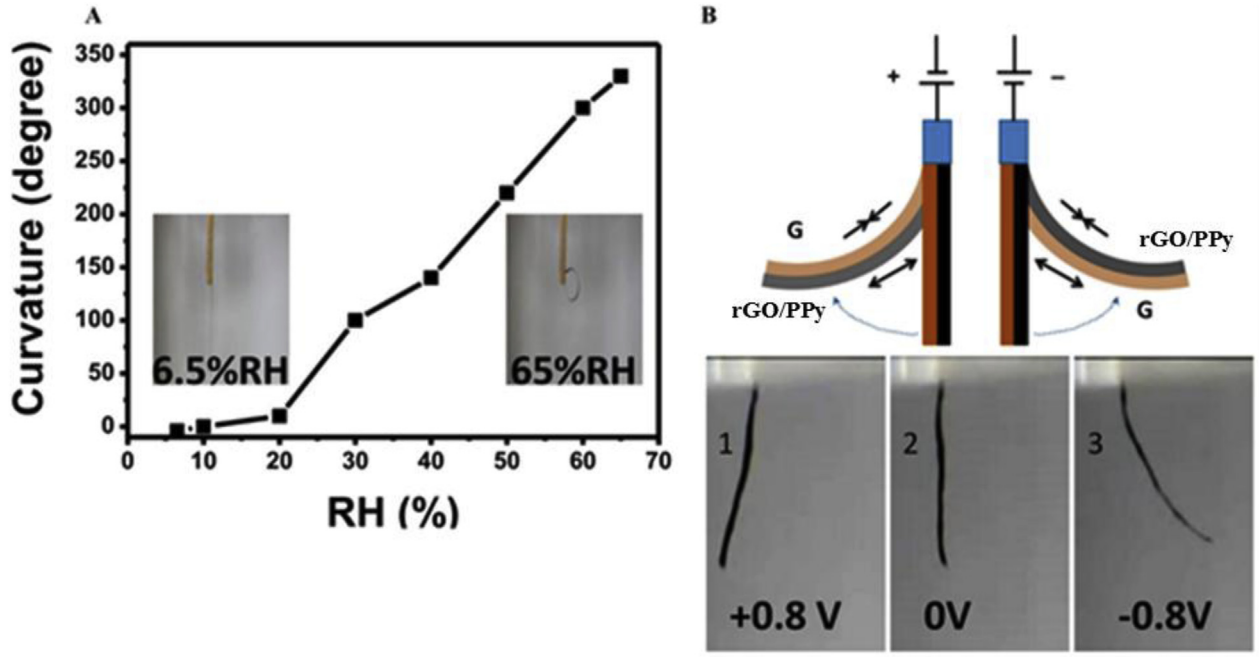

Fig. 11. (A) Plot of the curvature of rGO/PPy film versus RH. The insets are photographs of the rGO/PPy film under different humidities. (B) Actuation mechanism of the asymmetric rGO/PPy film and photographs of the bending status for the rGO/PPy film actuator driven by the electrochemical potential within ±0.8 V. The rGO/PPy sides are placed on the right and left sides in the demo actuator to control the direction of actuation with the corresponding potentials of +0.8 V (1), 0 V (2), and −0.8 V (3), respectively. Reproduced by permissions of the American Chemical Society [135].

adsorbs the light. As a result of GO and BOPP's difference in coefficient of thermal expansions (0.85 ppm K^{-1} for GO and 137 ppm K^{-1} for BOPP), the films would bend upon exposure to NIR light. When exposed on the BOPP side the actuator would bend towards the GO side within 10 s with a bending curvature of 2.8 cm^{-1}.

Ji et al. [134] developed a similar bilayer actuator responding to humidity and NIR with a polydopamine-modified rGO layer and a Norland Optical Adhesive (NOA)-63 layer. The NOA is responsive to neither humidity or NIR, thus imbuing the bilayer actuator with fast and reversible bending and unbending under the stimuli. The film rolled up at 7% RH and unrolled when exposed to 80% RH in 46 s and showed reversible rolling up in 53 s when returned to 7% RH for at least 7 cycles. The authors were also able to develop a walking device driven by NIR, by attaching PET plates onto opposite ends of the film with a complete cycle of bending and unbending taking 3.8 s and moving ~4–5 mm per cycle.

GO-based multi-stimuli-responsive actuators are not just limited to humidity and NIR. Jiang et al. [135] formed a nanocomposite actuator with rGO and polypyrrole (PPy) that responds to humidity and electro-mechanical stimuli. The authors used a self-oxidation reduction strategy to form the film in which GO acted as the oxidant to polymerize pyrrole into PPy, thus being partially reduced and forming cross-links between rGO and PPy. At low RH, the film exhibited little to no curvature; as the RH was raised, the film curled up and reached a maximum curvature of 330° at an RH of 65% (Fig. 11A). The actuator could also be driven by electrochemical potential, actuating to both sides depending upon the potential applied, as shown in Fig. 11B.

The above results suggest the versatile nature of GO-based actuators, offering a promising material for stimuli-responsive actuation. The diverse properties of GO will allow for the development and incorporation of GO into multi-stimuli-responsive smart materials for use in highly humid environments and touchless sensing technology with electromechanical responses.

4.3. Corrosion resistance

Graphene derivatives show promise for anti-corrosive polymer coatings thanks to their 2D morphology and high chemical inertness [12,15]. Polymers alone are permeable to chloride, sulfites, water and other chemicals that would be harmful to substrate metals [136], but graphene and its derivatives could be used as fillers to prevent the diffusion of harmful materials to a metal surface or even promote the generation of a passivation layer [137].

Ghauri et al. compared the abilities of GO (by improved Hummer's method) and rGO (by hydrazine reduction) in epoxy nanocomposites on steel substrates [15]. Electrical impedance spectroscopy (EIS) showed that the modulus of impedance (|Z|) of the GO coating was 6.36 kΩ cm^2 and that of the rGO coating was 3.48 kΩ cm^2 after 24 h of exposure to a Cl^- ion electrolyte flux. rGO showed a higher resistivity to electrolyte flux after 1 h due to its hydrophobicity and closer interlayer spacing; however, because the rGO was more conductive than GO for migration of Cl^- and Fe^{3+} ions through the coating and at the metal/coating interface, which might accelerate the process of a subsequent accumulation of

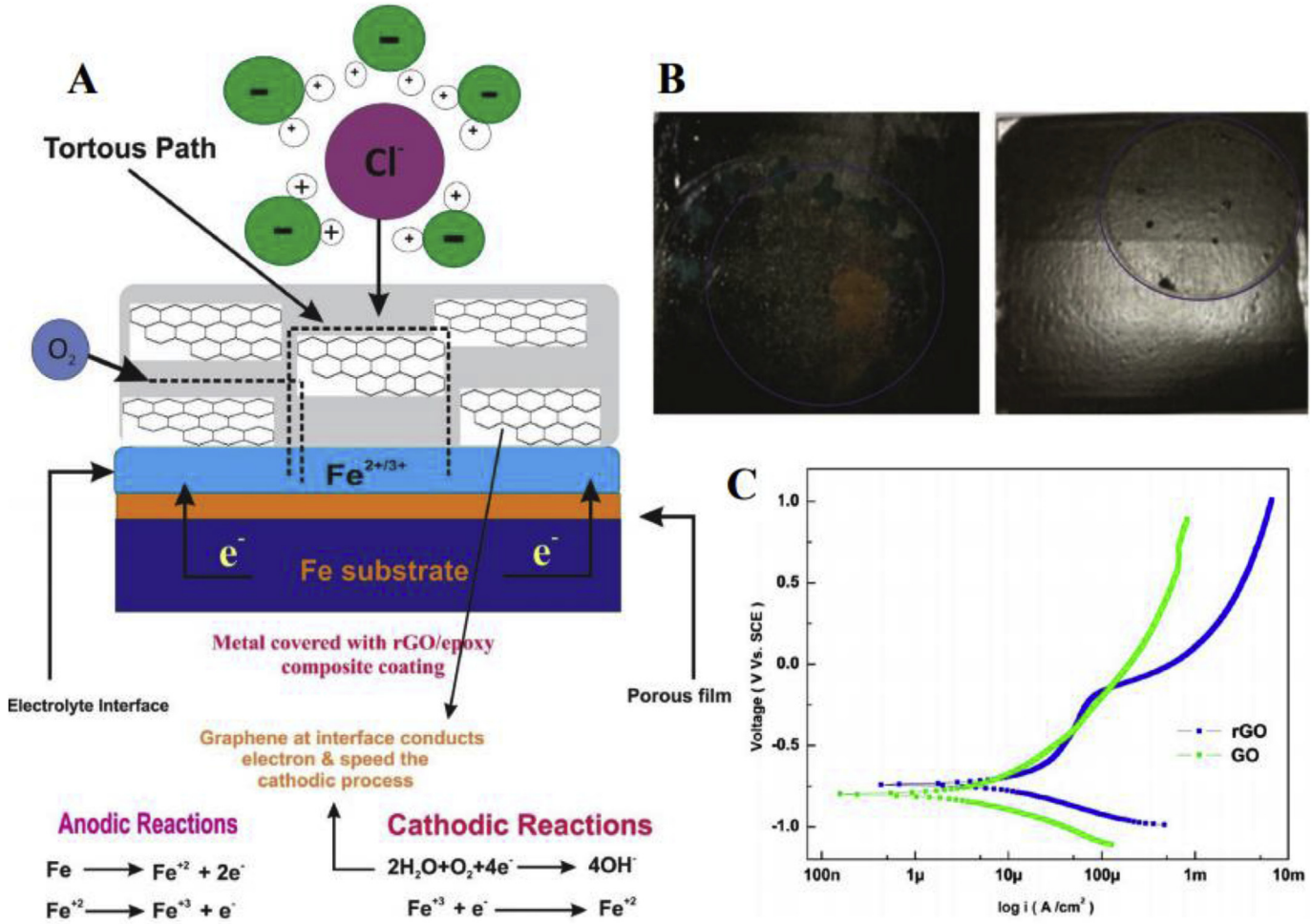

Fig. 12. (A) Schematic of electrochemical response of rGO coatings in chloride containing media. (B) Photographs of coatings after electrochemical tests: rGO (left) and GO (right). (C) Potentiodynamic polarization plots of the coatings after 24 h immersion in 3.5% NaCl solution. Reproduced with permission from IOP Publishing [15].

corrosion products (Fig. 12A). The study determined that GO was better than rGO at providing long-term corrosion protection for the steel substrates. A Tafel fit of potentiodynamic polarization, as well as images of the coatings after 24 h of exposure, showed a much lower corrosion current density for GO (4.86 μA cm^{-2}) than for rGO (28.60 μA cm^{-2}), as well as no corrosion product formed on the GO-coated steel (Fig. 12B and C).

Singhbabu et al. proposed that the largest obstacle to reliable graphene oxide corrosion barriers is defect formation [16]. They reflected on several studies done by other groups and developed a methodology of deriving rGO from shellac bio-polymer. Citing the previous literature where the heating of shellac bio-polymer in an inert atmosphere resulted in graphene oxide, they directly dip-coated cold rolled steel (CRS) with shellac solution in isopropanol, then heated the coating in a hydrogen atmosphere at 710 °C for 24 h. To prevent exposure of the metal surface to any defects in the resulting coating, they dipped the coated metal once again in the shellac solution and cured it at 350 °C in air for 10 min (Fig. 13A). They verified the existence of an rGO layer by Raman spectroscopy, XPS, and TEM. While they found that this method produces many defects in the rGO coating and that the 2nd dipping step was crucial to seal the pores generated by the annealing process, they also found that the impermeable behavior of rGO makes a substantial contribution to the CRS sheets. They calculate a corrosion current density 10,000 times smaller for coated CRS ($1.40 \times 10^{-9} \pm 2.80 \times 10^{-10}$ A cm^{-2}) than for bare CRS ($1.58 \times 10^{-5} \pm 1.78 \times 10^{-6}$ A cm^{-2}) using a Tafel fit (Fig. 13B).

While GO has shown promise in anti-corrosion coatings, much work still needs to be done to form a long-lasting, defect-free corrosion barrier. A recent article by Cui et al. warns against this area of research [138]. As they claim, and as Singhbabu's example demonstrates, graphene coatings would need to be completely defect- and pinhole-free to prevent galvanic corrosion, which has been demonstrated to be a non-trivial act. Besides, once damaged, a single- or multi-layered graphene would not be able to prevent corrosion due to its cathodic nature. A possible solution would be to create a graphene-polymer nanocomposite in which graphene was perfectly dispersed and which had scratch-resistant and/or self-healing properties, but this remains a challenge for anti-corrosive coatings for metals.

4.4. Energy storage

With rGO's superior electrical properties, rGO has become a promising material for many energy applications, such as in supercapacitors [139–142], lithium ion batteries (LIBs) [143–146], and stretchable electronics [71,147,148]. In this review, we will highlight some of the recent advancements made in the energy storage field utilizing rGO materials. For further review on energy applications, the authors would direct the readers to the review by El-Kady and co-workers [149].

Because of their long cycle lifetime and high-power density, supercapacitors have become a highly important area of research for energy storage devices. As such, it is no surprise that rGO materials have become important to the recent study of supercapacitors. A problem with GO is that it will tend to agglomerate during processing, greatly reducing its theoretical high surface area thus limiting its supercapacitance performance. Xu et al. [150] was able to design a sponge templated GO supercapacitor electrode by combining GO with a PU sponge. This material exhibited a specific capacitance of 401 F g^{-1} in aqueous electrolytes and an energy density of 89 W h kg^{-1} due to creating a shorter ion transport distance with the 3D structure and inner porosity. Zhao et al. [151] designed a supercapacitor electrode of GO/NaCl/Urea film, which upon hydrothermal treatment was reduced to rGO. During the hydrothermal treatment the NaCl acts to prohibit restacking of the graphene sheets and urea results in nitrogen doping improving the capacitance over rGO alone. The film exhibited a specific capacitance of 425 F g^{-1} and a volumetric specific capacitance of 693 F cm^{-3} at 1 A g^{-1} in 1 M H_2SO_4.

In other energy storage applications, rGO based materials have found success in LIBs [152,153]. Wang et al. [154] reported a method to design folded paper like rGO electrode decorated with Tin Oxide (SnO_2) for use as the electrode for LIBs. Fig. 14A shows a schematic illustration comparing the folded electrode to the general thick film electrode. The thick film electrode will show poor electron/ion transport kinetics limiting the electrochemical reaction between the active materials and the lithium ion. While the folded electrode provided new paths for free electron flow and built in voids for superior Li^+ transport kinetics. For the folded electrode there was a small increase in resistance of 0.5–5.6% between the non-folded and folded rGO/SnO_2 film, indicating that the folded structure maintained comparable in-plane electrical conductivity to flat films. The folded electrode was combined as an anode with a $LiCoO_2$ cathode and was tested at extended cycles at a rate of 0.5 C (1.70 mA cm^{-2}) (Fig. 14B). The fold electrode showed a cycle life up to 500 with a capacity retention of 73.7% and an end areal capacity of 2.53 mAh cm^{-2}. The cell retained its capacity as high as 89.2% of the initial value after 200 cycles (Fig. 14C) and maintained areal capacities in the range of portable devices showing the viability to use rGO in commercial devices.

Besides LIBs, rGO has also been shown to work with sodium-ion batteries (SIBs), which are a potential alternative to lithium due to lower environmental impact and lower cost [155]. Wang et al. [156] combined VS_4 with rGO as an effective nanocomposite anode for SIBs. The authors explored two procedures to achieve high-specific capacity and stable cycling performances. They were able to control the microstructure by connecting the VS_4 with rGO in a loose stack architecture, increasing the pseudocapacitive charge storage to improve the kinetics of sodiation/desodiation for the VS_4/rGO anode. The material showed a specific charge capacity of 580 mAh g^{-1} at 0.1 A g^{-1} and after 300 cycles showed a retention of 98% at 0.5 A g^{-1}. It was found that a porous stack microstructure of the VS_4/rGO could be obtained by controlling the rGO contents, which improved the pseudocapacitive charge storage by enabling more active surface sites.

Wei et al. [157] was able to combine both functionalities of LIBs and supercapacitors by designing a polyoxometalates based metal organic framework (POMOFs) with rGO into a battery-supercapacitor hybrid. By taking advantage of the individual properties of polyoxometalates (POMs), metal organic frameworks (MOFs), and rGO, which exhibit high electron uptake, high capacitances, and high electronic conductivity, respectively, the POMOFs/rGO nanocomposite exhibited high reversible capacity, good rate capability, and excellent cycling stability. This new material was found to have a reversible capacity of 1075 mAh g^{-1} over 100 cycles at 50 mA g^{-1} and a capacity retention approaching 100% at 2000 and 3000 mA g^{-1} after 400 cycles. The proposed reasons for this material exhibiting both battery and supercapacitor behavior is as follows: the battery performance is a result of Li^+ coordination with the organic component of the MOFs and through redox interactions of the metal ions in the POMs; the capacitive behaviors are a result of storing Li^+ in available interstitial sites at the interface or pores of the POMOFs, which are charge compensated by additional electrons on the surface of rGO.

5. Conclusion and outlook

In this article, we summarize the recent progress in synthesizing graphene and its derivatives, the effect of synthesis on the properties of the materials, and the promising applications related to those properties. Because of the highly tunable nature of GO and rGO, a diverse range of mechanical, electrical, and thermal properties can be achieved and effectively incorporated into nanocomposite materials. GO and rGO can be used in a broad range of applications and show promise as an integral material to the progression of new and improved products. While the focus of this article was on only a selected few applications (membranes/coating, stimuli-responsive materials, anticorrosion, and energy storage), the use of GO and rGO could also motivate the development and design of many other applications, including sensors [40,158,159],

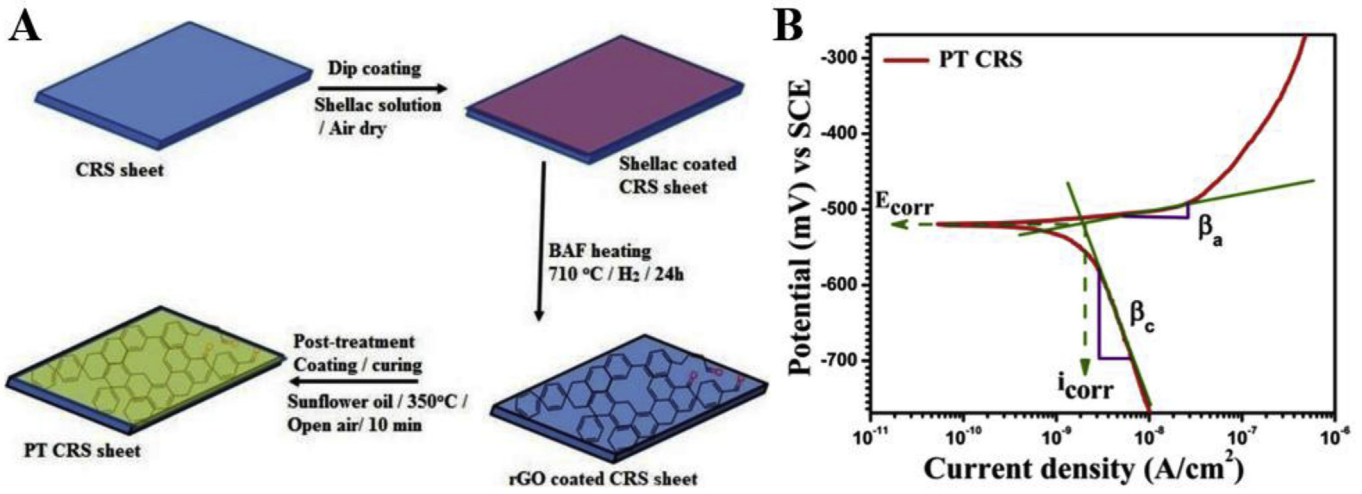

Fig. 13. (A) Schematic diagram for the production of rGO coated CRS sheet (A4 size) using an industrial batch annealing furnace. (B) Tafel plot with anodic and cathodic slopes of coated PT CRS sheets. Reproduced with permission from Elsevier [16].

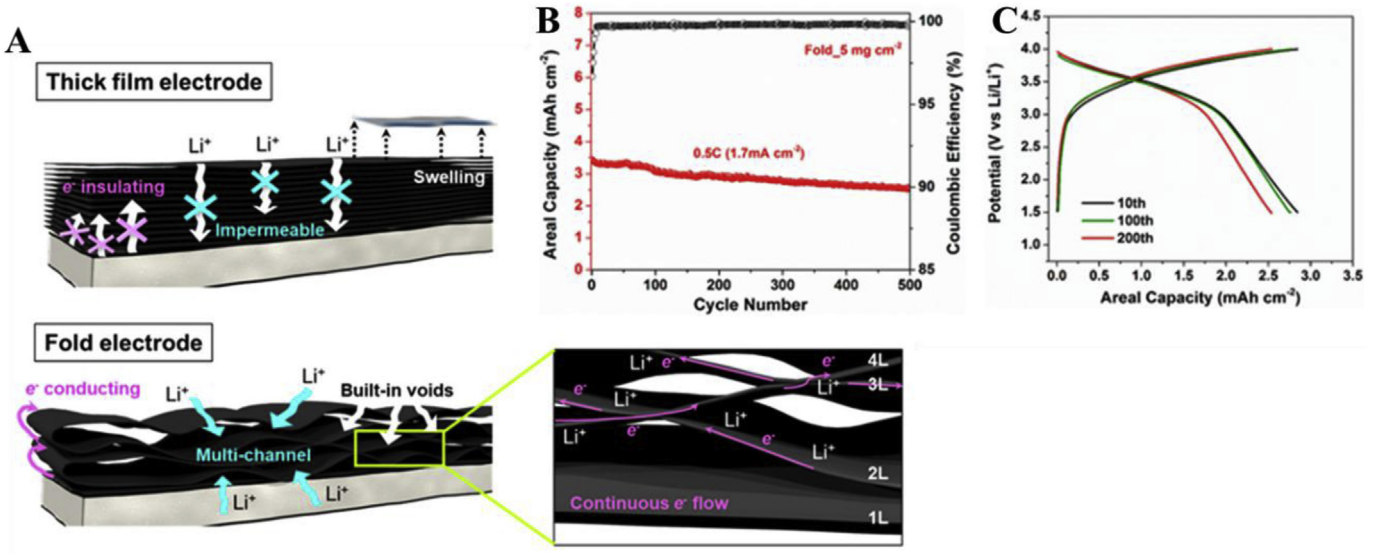

Fig. 14. (A) Schematic illustration showing the configuration of a "film electrode" and a "folded electrode". (B) Long-term cycle performance of the Fold_5 (areal density of ~5 mg cm^{-2}) electrode at 0.5 C rate. (C) The charge/discharge profiles of the Fold_5-LCO (LiCoO2) full cell at 0.5 C rate. Reproduced with permission from the American Chemical Society [154].

photoluminescence [23], electronics [57,160], energy [161,162], and catalysis [41,163,164].

Although significant progress has been made, many challenges still need to be addressed for full incorporation of GO and rGO into industrial applications. Even though the current synthetic pathways are encouraging for the generation of large-scale production of the materials, the control and refinement of particles with the same properties need to be further explored. While on average the properties can be improved through the various methods outlined, uniform properties will be key to the development of real-world applications as industrial products need to be highly reproducible. In addition, several unique techniques are highlighted to show the potential of using GO in many applications, with the key to the exceptional functionalities being related to fabrication techniques that are unscalable, expensive, and time-consuming. Further exploration needs to be conducted to fabricate nanocomposites through simple common industrial means without sacrificing the exceptional properties of the GO.

Acknowledgements

This research was sponsored by the National Science Foundation (NSF, CMMI-1562907). A.T.S. acknowledges the GAANN Fellowship for financial support (No. P200A150330). A.M.L. acknowledges the Navy STEM Fellowship and the GAANN Fellowship for financial support.

References

[1] C. Lee, X. Wei, J.W. Kysar, J. Hone, Measurement of the elastic properties and intrinsic strength of monolayer graphene, Science 321 (5887) (2008) 385–388.
[2] T. Kuilla, S. Bhadra, D. Yao, N.H. Kim, S. Bose, J.H. Lee, Recent advances in graphene based polymer composites, Prog. Polym. Sci. 35 (11) (2010) 1350–1375.
[3] Y. Cui, S.I. Kundalwal, S. Kumar, Gas Barrier Performance of Graphene/polymer Nanocomposites, Pergamon, 2016, pp. 313–333.
[4] L. Sun, M. Xiao, J. Liu, K. Gong, A study of the polymerization of styrene initiated by K-THF-GIC system, Eur. Polym. J. 42 (2) (2006) 259–264.
[5] M. Xiao, L. Sun, J. Liu, Y. Li, K. Gong, Synthesis and properties of polystyrene/graphite nanocomposites, Polymer 43 (8) (2002) 2245–2248.

[6] Y. Li, J. Zhu, S. Wei, J. Ryu, Q. Wang, L. Sun, Z. Guo, Poly(propylene) nanocomposites containing various carbon nanostructures, Macromol. Chem. Phys. 212 (22) (2011) 2429–2438.
[7] Y. Li, J. Zhu, S. Wei, J. Ryu, L. Sun, Z. Guo, Poly(propylene)/Graphene nanoplatelet nanocomposites: melt rheological behavior and thermal, Electric. Electron. Prop., Macromol. Chem. Phys. 212 (18) (2011) 1951–1959.
[8] Y. Zhu, S. Murali, W. Cai, X. Li, J.W. Suk, J.R. Potts, R.S. Ruoff, Graphene and graphene oxide: synthesis, properties, and applications, Adv. Mater. 22 (35) (2010) 3906–3924.
[9] S. Niyogi, E. Bekyarova, M.E. Itkis, J.L. McWilliams, M.A. Hamon, R.C. Haddon, Solution properties of graphite and graphene, J. Am. Chem. Soc. 128 (24) (2006) 7720–7721.
[10] F. Pendolino, N. Armata, Graphene Oxide in Environmental Remediation Process, 2017.
[11] S. Pei, H.M. Cheng, The Reduction of Graphene Oxide, 2012, pp. 3210–3228.
[12] B.M. Yoo, H.J. Shin, H.W. Yoon, H.B. Park, Graphene and graphene oxide and their uses in barrier polymers, J. Appl. Polym. Sci. 131 (1) (2014) (n/a-n/a).
[13] C. Cheng, S. Li, A. Thomas, N.A. Kotov, R. Haag, Functional graphene nanomaterials based architectures: biointeractions, fabrications, and emerging biological applications, Chem. Rev. 117 (3) (2017) 1826–1914.
[14] B. Tan, N.L. Thomas, A review of the water barrier properties of polymer/clay and polymer/graphene nanocomposites, J. Membr. Sci. 514 (2016) 595–612.
[15] F.A. Ghauri, M.A. Raza, M.S. Baig, S. Ibrahim, Corrosion study of the graphene oxide and reduced graphene oxide-based epoxy coatings, Mater. Res. Express 4 (12) (2017), 125601-125601.
[16] Y.N. Singhbabu, B. Sivakumar, S.K. Choudhary, S. Das, R.K. Sahu, Corrosion-protective reduced graphene oxide coated cold rolled steel prepared using industrial setup: a study of protocol feasibility for commercial production, Surf. Coating. Technol. 349 (2018) 119–132.
[17] K. Huang, G. Liu, Y. Lou, Z. Dong, J. Shen, W. Jin, A graphene oxide membrane with highly selective molecular separation of aqueous organic solution, Angew. Chem. 126 (27) (2014) 7049–7052.
[18] R.K. Joshi, S. Alwarappan, M. Yoshimura, V. Sahajwalla, Y. Nishina, Graphene oxide: the new membrane material, Applied Materials Today 1 (1) (2015) 1–12.
[19] S. Sun, P. Wu, A one-step strategy for thermal- and pH-responsive graphene oxide interpenetrating polymer hydrogel networks, J. Mater. Chem. 21 (12) (2011) 4095–4097.
[20] Y. Chen, P. Xu, Z. Shu, M. Wu, L. Wang, S. Zhang, Y. Zheng, H. Chen, J. Wang, Y. Li, J. Shi, Multifunctional graphene oxide-based triple stimuli-responsive nanotheranostics, Adv. Funct. Mater. 24 (28) (2014) 4386–4396.
[21] S. Thakur, N. Karak, Multi-stimuli responsive smart elastomeric hyperbranched polyurethane/reduced graphene oxide nanocomposites, J. Mater. Chem. 2 (36) (2014) 14867–14875.
[22] C.K. Chua, M. Pumera, Chemical Reduction of Graphene Oxide: A Synthetic Chemistry Viewpoint, 2014, pp. 291–312.
[23] Z. Wang, J. Liu, W. Wang, H. Chen, Z. Liu, Q. Yu, H. Zeng, L. Sun, Aqueous phase preparation of graphene with low defect density and adjustable layers, Chem. Commun. 49 (92) (2013) 10835–10837.
[24] X.-Y. Wang, A. Narita, K. Müllen, Precision synthesis versus bulk-scale fabrication of graphenes, Nature Reviews Chemistry 2 (1) (2017), 0100-0100.
[25] B.C. Brodie, On the Atomic Weight of Graphite, The Royal Society, 1859, pp. 249–259.
[26] L. Staudenmaier, Verfahren zur Darstellung der Graphitsäure, Ber. Dtsch. Chem. Ges. 31 (2) (1898) 1481–1487.
[27] W.S. Hummers, R.E. Offeman, Preparation of graphitic oxide, J. Am. Chem. Soc. 80 (6) (1958), 1339-1339.
[28] N.J. Huang, J. Zang, G.D. Zhang, L.Z. Guan, S.N. Li, L. Zhao, L.C. Tang, Efficient interfacial interaction for improving mechanical properties of polydimethylsiloxane nanocomposites filled with low content of graphene oxide nanoribbons, RSC Adv. 7 (36) (2017) 22045–22053.
[29] N.I. Kovtyukhova, Layer-by-layer assembly of ultrathin composite films from micron-sized graphite oxide sheets and polycations, Chem. Mater. 11 (3) (1999) 771–778.
[30] L. Sun, B. Fugetsu, Mass production of graphene oxide from expanded graphite, Mater. Lett. 109 (2013) 207–210.
[31] R. Jalili, S.H. Aboutalebi, D. Esrafilzadeh, R.L. Shepherd, J. Chen, S. Aminorroaya-Yamini, K. Konstantinov, A.I. Minett, J.M. Razal, G.G. Wallace, Scalable one-step wet-spinning of graphene fibers and yarns from liquid crystalline dispersions of graphene oxide: towards multifunctional textiles, Adv. Funct. Mater. 23 (43) (2013) 5345–5354.
[32] D.C. Marcano, D.V. Kosynkin, J.M. Berlin, A. Sinitskii, Z. Sun, A. Slesarev, L.B. Alemany, W. Lu, J.M. Tour, Improved synthesis of graphene oxide, ACS Nano 4 (8) (2010) 4806–4814.
[33] J. Zhang, Q. Liu, Y. Ruan, S. Lin, K. Wang, H. Lu, Monolithic crystalline swelling of graphite oxide: a bridge to ultralarge graphene oxide with high scalability, Chem. Mater. 30 (6) (2018) 1888–1897.
[34] L. Dong, Z. Chen, X. Zhao, J. Ma, S. Lin, M. Li, Y. Bao, L. Chu, K. Leng, H. Lu, K.P. Loh, A non-dispersion strategy for large-scale production of ultra-high concentration graphene slurries in water, Nat. Commun. 9 (1) (2018) 76.
[35] S. Stankovich, D.A. Dikin, R.D. Piner, K.A. Kohlhaas, A. Kleinhammes, Y. Jia, Y. Wu, S.B.T. Nguyen, R.S. Ruoff, Synthesis of graphene-based nanosheets via chemical reduction of exfoliated graphite oxide, Carbon 45 (7) (2007) 1558–1565.
[36] K.K.H. De Silva, H.H. Huang, R.K. Joshi, M. Yoshimura, Chemical Reduction of Graphene Oxide Using Green Reductants, 2017, pp. 190–199.
[37] G. Williams, B. Seger, P.V. Kamt, TiO2-graphene nanocomposites. UV-assisted photocatalytic reduction of graphene oxide, ACS Nano 2 (7) (2008) 1487–1491.
[38] S. Yang, M.R. Lohe, K. Müllen, X. Feng, New-generation graphene from electrochemical approaches: production and applications, Adv. Mater. 28 (29) (2016) 6213–6221.
[39] S. Pei, H.-M. Cheng, The reduction of graphene oxide, Carbon 50 (9) (2012) 3210–3228.
[40] L. Li, G. Wu, G. Yang, J. Peng, J. Zhao, J.J. Zhu, Focusing on Luminescent Graphene Quantum Dots: Current Status and Future Perspectives, 2013, pp. 4015–4039.
[41] J.P. Melo, P.L. Ríos, P. Povea, C. Morales-Verdejo, M.B. Camarada, Graphene oxide quantum dots as the support for the synthesis of gold nanoparticles and their applications as new catalysts for the decomposition of composite solid propellants, ACS Omega 3 (7) (2018) 7278–7287.
[42] P. Tian, L. Tang, K.S. Teng, S.P. Lau, Graphene quantum dots from chemistry to applications, Materials Today Chemistry 10 (2018) 221–258.
[43] Q. Lu, C. Wu, D. Liu, H. Wang, W. Su, H. Li, Y. Zhang, S. Yao, A facile and simple method for synthesis of graphene oxide quantum dots from black carbon, Green Chem. 19 (4) (2017) 900–904.
[44] W. Wang, Z. Wang, J. Liu, Y. Peng, X. Yu, W. Wang, Z. Zhang, L. Sun, One-pot facile synthesis of graphene quantum dots from rice husks for Fe3+ sensing, Ind. Eng. Chem. Res. 57 (28) (2018) 9144–9150.
[45] P. Zhang, L. Ma, F. Fan, Z. Zeng, C. Peng, P.E. Loya, Z. Liu, Y. Gong, J. Zhang, X. Zhang, P.M. Ajayan, T. Zhu, J. Lou, Fracture toughness of graphene, Nat. Commun. 5 (2014).
[46] J.W. Suk, R.D. Piner, J. An, R.S. Ruoff, Mechanical properties of monolayer graphene oxide, ACS Nano 4 (11) (2010) 6557–6564.
[47] C. Gómez-Navarro, M. Burghard, K. Kern, Elastic properties of chemically derived single graphene sheets, Nano Lett. 8 (7) (2008) 2045–2049.
[48] H. Kim, A.A. Abdala, C.W. Macosko, Graphene/Polymer Nanocomposites, Macromol. 43 (16) (2010) 6515–6530.
[49] T. Cheng-An, Z. Hao, W. Fang, Z. Hui, Z. Xiaorong, W. Jianfang, Mechanical properties of graphene oxide/polyvinyl alcohol composite film, Polym. Polym. Compos. 25 (1) (2017) 11–16.
[50] S. Jiang, Z. He, Q. Li, J. Wang, G. Wu, Y. Zhao, M. Kang, Effect of Carbon Fiber-Graphene Oxide Multiscale Reinforcements on the Thermo-Mechanical Properties of Polyurethane Elastomer, Polymer Composites, Wiley-Blackwell, 2018.
[51] C. Bao, L. Song, W. Xing, B. Yuan, C.A. Wilkie, J. Huang, Y. Guo, Y. Hu, Preparation of graphene by pressurized oxidation and multiplex reduction and its polymer nanocomposites by masterbatch-based melt blending, J. Mater. Chem. 22 (13) (2012) 6088–6096.
[52] K.S. Novoselov, V.I. Fal'ko, L. Colombo, P.R. Gellert, M.G. Schwab, K. Kim, A roadmap for graphene, Nature 490 (2012) 192.
[53] S. Park, R.S. Ruoff, Chemical methods for the production of graphenes, Nat. Nanotechnol. 4 (2009) 217.
[54] S. Stankovich, D.A. Dikin, G.H.B. Dommett, K.M. Kohlhaas, E.J. Zimney, E.A. Stach, R.D. Piner, S.T. Nguyen, R.S. Ruoff, Graphene-based composite materials, Nature 442 (2006) 282.
[55] Z. Wang, J.K. Nelson, H. Hillborg, S. Zhao, L.S. Schadler, Graphene oxide filled nanocomposite with novel electrical and dielectric properties, Adv. Mater. 24 (23) (2012) 3134–3137.
[56] L. Tang, X. Li, R. Ji, K.S. Teng, G. Tai, J. Ye, C. Wei, S.P. Lau, Bottom-up synthesis of large-scale graphene oxide nanosheets, J. Mater. Chem. 22 (12) (2012) 5676–5683.
[57] G. Eda, G. Fanchini, M. Chhowalla, Large-area ultrathin films of reduced graphene oxide as a transparent and flexible electronic material, Nat. Nanotechnol. 3 (2008) 270.
[58] S. Pei, J. Zhao, J. Du, W. Ren, H.-M. Cheng, Direct reduction of graphene oxide films into highly conductive and flexible graphene films by hydrohalic acids, Carbon 48 (15) (2010) 4466–4474.
[59] A. Bagri, C. Mattevi, M. Acik, Y.J. Chabal, M. Chhowalla, V.B. Shenoy, Structural evolution during the reduction of chemically derived graphene oxide, Nat. Chem. 2 (2010) 581.
[60] S. Stankovich, D.A. Dikin, R.D. Piner, K.A. Kohlhaas, A. Kleinhammes, Y. Jia, Y. Wu, S.T. Nguyen, R.S. Ruoff, Synthesis of graphene-based nanosheets via chemical reduction of exfoliated graphite oxide, Carbon 45 (7) (2007) 1558–1565.
[61] D. Voiry, J. Yang, J. Kupferberg, R. Fullon, C. Lee, H.Y. Jeong, H.S. Shin, M. Chhowalla, High-quality graphene via microwave reduction of solution-exfoliated graphene oxide, Science 353 (6306) (2016) 1413–1416.
[62] P. Kumar, F. Shahzad, S. Yu, S.M. Hong, Y.-H. Kim, C.M. Koo, Large-area reduced graphene oxide thin film with excellent thermal conductivity and electromagnetic interference shielding effectiveness, Carbon 94 (2015) 494–500.
[63] I.K. Moon, J. Lee, R.S. Ruoff, H. Lee, Reduced graphene oxide by chemical graphitization, Nat. Commun. 1 (2010) 73.
[64] L.L. Zhang, X. Zhao, M.D. Stoller, Y. Zhu, H. Ji, S. Murali, Y. Wu, S. Perales, B. Clevenger, R.S. Ruoff, Highly conductive and porous activated reduced graphene oxide films for high-power supercapacitors, Nano Lett. 12 (4) (2012) 1806–1812.
[65] M. Kim, C. Lee, J. Jang, Fabrication of highly flexible, scalable, and high-performance supercapacitors using polyaniline/reduced graphene oxide film with enhanced electrical conductivity and crystallinity, Adv. Funct. Mater. 24 (17) (2014) 2489–2499.
[66] M. Hou, M. Xu, B. Li, Enhanced electrical conductivity of cellulose nanofiber/graphene composite paper with a sandwich structure, ACS Sustain. Chem. Eng. 6 (3) (2018) 2983–2990.

[67] S. Wan, J. Peng, Y. Li, H. Hu, L. Jiang, Q. Cheng, Use of synergistic interactions to fabricate strong, tough, and conductive artificial nacre based on graphene oxide and chitosan, ACS Nano 9 (10) (2015) 9830–9836.
[68] H.-B. Zhang, W.-G. Zheng, Q. Yan, Y. Yang, J.-W. Wang, Z.-H. Lu, G.-Y. Ji, Z.-Z. Yu, Electrically conductive polyethylene terephthalate/graphene nanocomposites prepared by melt compounding, Polymer 51 (5) (2010) 1191–1196.
[69] S. Song, Y. Zhai, Y. Zhang, Bioinspired graphene oxide/polymer nanocomposite paper with high strength, toughness, and dielectric constant, ACS Appl. Mater. Interfaces 8 (45) (2016) 31264–31272.
[70] F. Li, J. Chen, X. Wang, M. Xue, G.F. Chen, Stretchable supercapacitor with adjustable volumetric capacitance based on 3D interdigital electrodes, Adv. Funct. Mater. 25 (29) (2015) 4601–4606.
[71] S. Wang, N. Liu, J. Su, L. Li, F. Long, Z. Zou, X. Jiang, Y. Gao, Highly stretchable and self-healable supercapacitor with reduced graphene oxide based fiber springs, ACS Nano 11 (2) (2017) 2066–2074.
[72] J.D. Renteria, S. Ramirez, H. Malekpour, B. Alonso, A. Centeno, A. Zurutuza, A.I. Cocemasov, D.L. Nika, A.A. Balandin, Strongly anisotropic thermal conductivity of free-standing reduced graphene oxide films annealed at high temperature, Adv. Funct. Mater. 25 (29) (2015) 4664–4672.
[73] C.B. Kim, J. Lee, J. Cho, M. Goh, Thermal conductivity enhancement of reduced graphene oxide via chemical defect healing for efficient heat dissipation, Carbon 139 (2018) 386–392.
[74] H. Im, J. Kim, Thermal conductivity of a graphene oxide–carbon nanotube hybrid/epoxy composite, Carbon 50 (15) (2012) 5429–5440.
[75] J. Kim, H. Im, J.-m. Kim, J. Kim, Thermal and electrical conductivity of Al(OH)3 covered graphene oxide nanosheet/epoxy composites, J. Mater. Sci. 47 (3) (2012) 1418–1426.
[76] S. Kim, J. Shimazu, T. Fukaminato, T. Ogata, S. Kurihara, Thermal conductivity of graphene oxide-enhanced polyvinyl alcohol composites depending on molecular interaction, Polymer 129 (2017) 201–206.
[77] G. Xue, J. Zhong, S. Gao, B. Wang, Correlation between the free volume and thermal conductivity of porous poly(vinyl alcohol)/reduced graphene oxide composites studied by positron spectroscopy, Carbon 96 (2016) 871–878.
[78] S. Song, Y. Zhang, Carbon nanotube/reduced graphene oxide hybrid for simultaneously enhancing the thermal conductivity and mechanical properties of styrene -butadiene rubber, Carbon 123 (2017) 158–167.
[79] A.L. Higginbotham, J.R. Lomeda, A.B. Morgan, J.M. Tour, Graphite oxide flame-retardant polymer nanocomposites, ACS Appl. Mater. Interfaces 1 (10) (2009) 2256–2261.
[80] B. Yu, X. Wang, X. Qian, W. Xing, H. Yang, L. Ma, Y. Lin, S. Jiang, L. Song, Y. Hu, S. Lo, Functionalized graphene oxide/phosphoramide oligomer hybrids flame retardant prepared via in situ polymerization for improving the fire safety of polypropylene, RSC Adv. 4 (60) (2014) 31782–31794.
[81] X. Wang, L. Song, H. Yang, W. Xing, B. Kandola, Y. Hu, Simultaneous reduction and surface functionalization of graphene oxide with POSS for reducing fire hazards in epoxy composites, J. Mater. Chem. 22 (41) (2012) 22037–22043.
[82] B. Yu, Y. Shi, B. Yuan, S. Qiu, W. Xing, W. Hu, L. Song, S. Lo, Y. Hu, Enhanced thermal and flame retardant properties of flame-retardant-wrapped graphene/epoxy resin nanocomposites, J. Mater. Chem. 3 (15) (2015) 8034–8044.
[83] X. Zhang, Q. Shen, X. Zhang, H. Pan, Y. Lu, Graphene oxide-filled multilayer coating to improve flame-retardant and smoke suppression properties of flexible polyurethane foam, J. Mater. Sci. 51 (23) (2016) 10361–10374.
[84] B. Wicklein, A. Kocjan, G. Salazar-Alvarez, F. Carosio, G. Camino, M. Antonietti, L. Bergström, Thermally insulating and fire-retardant lightweight anisotropic foams based on nanocellulose and graphene oxide, Nat. Nanotechnol. 10 (2014) 277.
[85] Y.-H. Yang, L. Bolling, M.A. Priolo, J.C. Grunlan, Super gas barrier and selectivity of graphene oxide-polymer multilayer thin films, Adv. Mater. 25 (4) (2013) 503–508.
[86] Y. Su, V.G. Kravets, S.L. Wong, J. Waters, A.K. Geim, R.R. Nair, Impermeable barrier films and protective coatings based on reduced graphene oxide, Nat. Commun. 5 (2014) 4843.
[87] A. Ammar, A.M. Al-Enizi, M.A.A. AlMaadeed, A. Karim, Influence of Graphene Oxide on Mechanical, Morphological, Barrier, and Electrical Properties of Polymer Membranes, 2016, pp. 274–286.
[88] L. Sun, W.J. Boo, A. Clearfield, H.-J. Sue, H.Q. Pham, Barrier properties of model epoxy nanocomposites, J. Membr. Sci. 318 (1–2) (2008) 129–136.
[89] L. Sun, H.-J. Sue, Permeation properties of epoxy nanocomposites, in: V. Mittal (Ed.), Barrier Properties of Polymer Clay Nanocomposites, Nova Science Publishers, New York, USA, 2010, pp. 73–93.
[90] H.-J. Sue, K.T. Gam, N. Bestaoui, A. Clearfield, M. Miyamoto, N. Miyatake, Fracture behavior of α-zirconium phosphate-based epoxy nanocomposites, Acta Mater. 52 (8) (2004) 2239–2250.
[91] W.J. Boo, L. Sun, J. Liu, E. Moghbelli, A. Clearfield, H.-J. Sue, H. Pham, N. Verghese, Effect of nanoplatelet dispersion on mechanical behavior of polymer nanocomposites, J. Polym. Sci. B Polym. Phys. 45 (12) (2007) 1459–1469.
[92] J. Yu, J. Liu, A. Clearfield, J.E. Sims, M.T. Speiegle, S.L. Suib, L. Sun, Synthesis of layered double hydroxide single-layer nanosheets in formamide, Inorg. Chem. 55 (22) (2016) 12036–12041.
[93] J. Liu, Nanostructured Multi-Functional Hybrid Nanocoatings from One-step Coassembly, Doctoral Dissertations, 2018.
[94] A. Kausar, Composite coatings of polyamide/graphene: microstructure, mechanical, thermal, and barrier properties, Compos. Interfac. 25 (2) (2018) 109–125.
[95] D. Pierleoni, M. Minelli, S. Ligi, M. Christian, S. Funke, N. Reineking, V. Morandi, F. Doghieri, V. Palermo, Selective gas permeation in graphene oxide-polymer self-assembled multilayers, ACS Appl. Mater. Interfaces 10 (13) (2018) 11242–11250.
[96] F. Ding, J. Liu, S. Zeng, Y. Xia, K.M. Wells, M.-P. Nieh, L. Sun, Biomimetic nanocoatings with exceptional mechanical, barrier, and flame-retardant properties from large-scale one-step coassembly, Science Advances 3 (7) (2017).
[97] H. Li, Z. Song, X. Zhang, Y. Huang, S. Li, Y. Mao, H.J. Ploehn, Y. Bao, M. Yu, Ultrathin, molecular-sieving graphene oxide membranes for selective hydrogen separation, Science 342 (6154) (2013) 95–98.
[98] J. Shen, G. Liu, K. Huang, Z. Chu, W. Jin, N. Xu, Subnanometer two-dimensional graphene oxide channels for ultrafast gas sieving, ACS Nano 10 (3) (2016) 3398–3409.
[99] H.W. Kim, H.W. Yoon, S.-M. Yoon, B.M. Yoo, B.K. Ahn, Y.H. Cho, H.J. Shin, H. Yang, U. Paik, S. Kwon, J.-Y. Choi, H.B. Park, Selective gas transport through few-layered graphene and graphene oxide membranes, Science 342 (6154) (2013) 91–95.
[100] H.B. Park, C.H. Jung, Y.M. Lee, A.J. Hill, S.J. Pas, S.T. Mudie, E. Van Wagner, B.D. Freeman, D.J. Cookson, Polymers with cavities tuned for fast selective transport of small molecules and ions, Science 318 (5848) (2007) 254–258.
[101] N. Du, H.B. Park, G.P. Robertson, M.M. Dal-Cin, T. Visser, L. Scoles, M.D. Guiver, Polymer nanosieve membranes for CO2-capture applications, Nat. Mater. 10 (2011) 372.
[102] D. Shekhawat, D.R. Luebke, H.W. Pennline, A Review of Carbon Dioxide Selective Membranes: A Topical Report, National Energy Technology Laboratory (NETL), Pittsburgh, PA, Morgantown, WV, and Albany, OR (United States), 2003. Medium: ED; Size: 1,040 pages.
[103] M. Hu, B. Mi, Enabling graphene oxide nanosheets as water separation membranes, Environ. Sci. Technol. 47 (8) (2013) 3715–3723.
[104] R.R. Nair, H.A. Wu, P.N. Jayaram, I.V. Grigorieva, A.K. Geim, Unimpeded permeation of water through helium-leak–tight graphene-based membranes, Science 335 (6067) (2012) 442–444.
[105] H. Huang, Z. Song, N. Wei, L. Shi, Y. Mao, Y. Ying, L. Sun, Z. Xu, X. Peng, Ultrafast viscous water flow through nanostrand-channelled graphene oxide membranes, Nat. Commun. 4 (2013) 2979.
[106] C.-N. Yeh, K. Raidongia, J. Shao, Q.-H. Yang, J. Huang, On the origin of the stability of graphene oxide membranes in water, Nat. Chem. 7 (2015) 166.
[107] K.H. Thebo, X. Qian, Q. Zhang, L. Chen, H.-M. Cheng, W. Ren, Highly stable graphene-oxide-based membranes with superior permeability, Nat. Commun. 9 (1) (2018) 1486.
[108] S. Bano, A. Mahmood, S.-J. Kim, K.-H. Lee, Graphene oxide modified polyamide nanofiltration membrane with improved flux and antifouling properties, J. Mater. Chem. 3 (5) (2015) 2065–2071.
[109] B. Tansel, Significance of thermodynamic and physical characteristics on permeation of ions during membrane separation: hydrated radius, hydration free energy and viscous effects, Separ. Purif. Technol. 86 (2012) 119–126.
[110] J. Abraham, K.S. Vasu, C.D. Williams, K. Gopinadhan, Y. Su, C.T. Cherian, J. Dix, E. Prestat, S.J. Haigh, I.V. Grigorieva, P. Carbone, A.K. Geim, R.R. Nair, Tunable sieving of ions using graphene oxide membranes, Nat. Nanotechnol. 12 (2017) 546.
[111] X. Song, Q. Zhou, T. Zhang, H. Xu, Z. Wang, Pressure-assisted preparation of graphene oxide quantum dot-incorporated reverse osmosis membranes: antifouling and chlorine resistance potentials, J. Mater. Chem. 4 (43) (2016) 16896–16905.
[112] Z. Zeng, D. Yu, Z. He, J. Liu, F.-X. Xiao, Y. Zhang, R. Wang, D. Bhattacharyya, T.T.Y. Tan, Graphene oxide quantum dots covalently functionalized PVDF membrane with significantly-enhanced bactericidal and antibiofouling performances, Sci. Rep. 6 (2016) 20142.
[113] A. Lukowiak, A. Kedziora, W. Strek, Antimicrobial graphene family materials: progress, advances, hopes and fears, Adv. Colloid Interface Sci. 236 (2016) 101–112.
[114] C. Zhang, K. Wei, W. Zhang, Y. Bai, Y. Sun, J. Gu, Graphene oxide quantum dots incorporated into a thin film nanocomposite membrane with high flux and antifouling properties for low-pressure nanofiltration, ACS Appl. Mater. Interfaces 9 (12) (2017) 11082–11094.
[115] M. Ma, L. Guo, D.G. Anderson, R. Langer, Bio-inspired polymer composite actuator and generator driven by water gradients, Science 339 (6116) (2013) 186–189.
[116] H. Arazoe, D. Miyajima, K. Akaike, F. Araoka, E. Sato, T. Hikima, M. Kawamoto, T. Aida, An autonomous actuator driven by fluctuations in ambient humidity, Nat. Mater. 15 (2016) 1084.
[117] Y. Qiu, M. Wang, W. Zhang, Y. Liu, Y.V. Li, K. Pan, An asymmetric graphene oxide film for developing moisture actuators, Nanoscale 10 (29) (2018) 14060–14066.
[118] Y. Zhang, H. Jiang, F. Li, Y. Xia, Y. Lei, X. Jin, G. Zhang, H. Li, Graphene oxide based moisture-responsive biomimetic film actuators with nacre-like layered structures, J. Mater. Chem. 5 (28) (2017) 14604–14610.
[119] J.T. Robinson, S.M. Tabakman, Y. Liang, H. Wang, H. Sanchez Casalongue, D. Vinh, H. Dai, Ultrasmall reduced graphene oxide with high near-infrared absorbance for photothermal therapy, J. Am. Chem. Soc. 133 (17) (2011) 6825–6831.
[120] C.-W. Lo, D. Zhu, H. Jiang, An infrared-light responsive graphene-oxide incorporated poly(N-isopropylacrylamide) hydrogel nanocomposite, Soft Matter 7 (12) (2011) 5604–5609.
[121] D.-K. Lim, A. Barhoumi, R.G. Wylie, G. Reznor, R.S. Langer, D.S. Kohane, Enhanced photothermal effect of plasmonic nanoparticles coated with reduced graphene oxide, Nano Lett. 13 (9) (2013) 4075–4079.
[122] E. Wang, M.S. Desai, S.-W. Lee, Light-controlled graphene-elastin composite hydrogel actuators, Nano Lett. 13 (6) (2013) 2826–2830.

[123] T. Wang, J. Huang, Y. Yang, E. Zhang, W. Sun, Z. Tong, Bioinspired smart actuator based on graphene oxide-polymer hybrid hydrogels, ACS Appl. Mater. Interfaces 7 (42) (2015) 23423–23430.
[124] Z. Cheng, T. Wang, X. Li, Y. Zhang, H. Yu, NIR–Vis–UV light-responsive actuator films of polymer-dispersed liquid crystal/graphene oxide nanocomposites, ACS Appl. Mater. Interfaces 7 (49) (2015) 27494–27501.
[125] H. Kim, J.H. Moon, T.J. Mun, T.G. Park, G.M. Spinks, G.G. Wallace, S.J. Kim, Thermally responsive torsional and tensile fiber actuator based on graphene oxide, ACS Appl. Mater. Interfaces 10 (38) (2018) 32760–32764.
[126] Q. Zhao, Y. Liang, L. Ren, Z. Yu, Z. Zhang, L. Ren, Bionic intelligent hydrogel actuators with multimodal deformation and locomotion, Nano Energy 51 (2018) 621–631.
[127] Y. Lian, Y. Liu, T. Jiang, J. Shu, H. Lian, M. Cao, Enhanced electromechanical performance of graphite oxide-nafion nanocomposite actuator, J. Phys. Chem. C 114 (21) (2010) 9659–9663.
[128] J. Liang, L. Huang, N. Li, Y. Huang, Y. Wu, S. Fang, J. Oh, M. Kozlov, Y. Ma, F. Li, R. Baughman, Y. Chen, Electromechanical actuator with controllable motion, fast response rate, and high-frequency resonance based on graphene and polydiacetylene, ACS Nano 6 (5) (2012) 4508–4519.
[129] X. Xie, L. Qu, C. Zhou, Y. Li, J. Zhu, H. Bai, G. Shi, L. Dai, An asymmetrically surface-modified graphene film electrochemical actuator, ACS Nano 4 (10) (2010) 6050–6054.
[130] C. Yang, Z. Liu, C. Chen, K. Shi, L. Zhang, X.-J. Ju, W. Wang, R. Xie, L.-Y. Chu, Reduced graphene oxide-containing smart hydrogels with excellent electro-response and mechanical properties for soft actuators, ACS Appl. Mater. Interfaces 9 (18) (2017) 15758–15767.
[131] W. Wang, D. Liu, Y. Liu, J. Leng, D. Bhattacharyya, Electrical actuation properties of reduced graphene oxide paper/epoxy-based shape memory composites, Compos. Sci. Technol. 106 (2015) 20–24.
[132] J. Kim, J.-H. Jeon, H.-J. Kim, H. Lim, I.-K. Oh, Durable and water-floatable ionic polymer actuator with hydrophobic and asymmetrically laser-scribed reduced graphene oxide paper electrodes, ACS Nano 8 (3) (2014) 2986–2997.
[133] L. Chen, M. Weng, P. Zhou, L. Zhang, Z. Huang, W. Zhang, Multi-responsive actuators based on a graphene oxide composite: intelligent robot and bioinspired applications, Nanoscale 9 (28) (2017) 9825–9833.
[134] M. Ji, N. Jiang, J. Chang, J. Sun, Near-infrared light-driven, highly efficient bilayer actuators based on polydopamine-modified reduced graphene oxide, Adv. Funct. Mater. 24 (34) (2014) 5412–5419.
[135] Y. Jiang, C. Hu, H. Cheng, C. Li, T. Xu, Y. Zhao, H. Shao, L. Qu, Spontaneous, straightforward fabrication of partially reduced graphene oxide–polypyrrole composite films for versatile actuators, ACS Nano 10 (4) (2016) 4735–4741.
[136] M. Stratmann, R. Feser, A. Leng, Corrosion protection by organic films, Electrochim. Acta 39 (8–9) (1994) 1207–1214.
[137] X. Luo, J. Zhong, Q. Zhou, S. Du, S. Yuan, Y. Liu, Cationic reduced graphene oxide as self-aligned nanofiller in the epoxy nanocomposite coating with excellent anticorrosive performance and its high antibacterial activity, ACS Appl. Mater. Interfaces 10 (21) (2018) 18400–18415.
[138] C. Cui, A.T.O. Lim, J. Huang, A Cautionary Note on Graphene Anti-corrosion Coatings, 2017, pp. 834–835.
[139] W.K. Chee, H.N. Lim, I. Harrison, K.F. Chong, Z. Zainal, C.H. Ng, N.M. Huang, Performance of flexible and binderless polypyrrole/graphene oxide/zinc oxide supercapacitor electrode in a symmetrical two-electrode configuration, Electrochim. Acta 157 (2015) 88–94.
[140] M. Wang, L.D. Duong, N.T. Mai, S. Kim, Y. Kim, H. Seo, Y.C. Kim, W. Jang, Y. Lee, J. Suhr, J.-D. Nam, All-solid-state reduced graphene oxide supercapacitor with large volumetric capacitance and ultralong stability prepared by electrophoretic deposition method, ACS Appl. Mater. Interfaces 7 (2) (2015) 1348–1354.
[141] X. Cao, B. Zheng, W. Shi, J. Yang, Z. Fan, Z. Luo, X. Rui, B. Chen, Q. Yan, H. Zhang, Reduced graphene oxide-wrapped MoO3 composites prepared by using metal–organic frameworks as precursor for all-solid-state flexible supercapacitors, Adv. Mater. 27 (32) (2015) 4695–4701.
[142] A. Lamberti, A. Gigot, S. Bianco, M. Fontana, M. Castellino, E. Tresso, C.F. Pirri, Self-assembly of graphene aerogel on copper wire for wearable fiber-shaped supercapacitors, Carbon 105 (2016) 649–654.
[143] D. Lin, Y. Liu, Z. Liang, H.-W. Lee, J. Sun, H. Wang, K. Yan, J. Xie, Y. Cui, Layered reduced graphene oxide with nanoscale interlayer gaps as a stable host for lithium metal anodes, Nat. Nanotechnol. 11 (2016) 626.
[144] J. Cao, C. Chen, Q. Zhao, N. Zhang, Q. Lu, X. Wang, Z. Niu, J. Chen, A flexible nanostructured paper of a reduced graphene oxide–sulfur composite for high-performance lithium–sulfur batteries with unconventional configurations, Adv. Mater. 28 (43) (2016) 9629–9636.
[145] J.-Q. Huang, T.-Z. Zhuang, Q. Zhang, H.-J. Peng, C.-M. Chen, F. Wei, Permselective graphene oxide membrane for highly stable and anti-self-discharge lithium–sulfur batteries, ACS Nano 9 (3) (2015) 3002–3011.
[146] K. Fu, Y. Wang, C. Yan, Y. Yao, Y. Chen, J. Dai, S. Lacey, Y. Wang, J. Wan, T. Li, Z. Wang, Y. Xu, L. Hu, Graphene oxide-based electrode inks for 3d-printed lithium-ion batteries, Adv. Mater. 28 (13) (2016) 2587–2594.
[147] K.S. Kim, Y. Zhao, H. Jang, S.Y. Lee, J.M. Kim, K.S. Kim, J.-H. Ahn, P. Kim, J.-Y. Choi, B.H. Hong, Large-scale pattern growth of graphene films for stretchable transparent electrodes, Nature 457 (2009) 706.
[148] H. Jang, Y.J. Park, X. Chen, T. Das, M.-S. Kim, J.H. Ahn, Graphene-based flexible and stretchable electronics, Adv. Mater. 28 (22) (2016) 4184–4202.
[149] M.F. El-Kady, Y. Shao, R.B. Kaner, Graphene for batteries, supercapacitors and beyond, Nat. Rev. Mater. 1 (2016) 16033.
[150] J. Xu, Z. Tan, W. Zeng, G. Chen, S. Wu, Y. Zhao, K. Ni, Z. Tao, M. Ikram, H. Ji, Y. Zhu, A hierarchical carbon derived from sponge-templated activation of graphene oxide for high-performance supercapacitor electrodes, Adv. Mater. 28 (26) (2016) 5222–5228.
[151] Y. Zhao, J. Liu, B. Wang, J. Sha, Y. Li, D. Zheng, M. Amjadipour, J. MacLeod, N. Motta, Supercapacitor electrodes with remarkable specific capacitance converted from hybrid graphene oxide/NaCl/urea films, ACS Appl. Mater. Interfaces 9 (27) (2017) 22588–22596.
[152] Y. Zhang, Q. Ma, S. Wang, X. Liu, L. Li, Poly(vinyl alcohol)-assisted fabrication of hollow carbon spheres/reduced graphene oxide nanocomposites for high-performance lithium-ion battery anodes, ACS Nano 12 (5) (2018) 4824–4834.
[153] Z. Sun, J. Zhang, L. Yin, G. Hu, R. Fang, H.-M. Cheng, F. Li, Conductive porous vanadium nitride/graphene composite as chemical anchor of polysulfides for lithium-sulfur batteries, Nat. Commun. 8 (2017) 14627.
[154] B. Wang, J. Ryu, S. Choi, G. Song, D. Hong, C. Hwang, X. Chen, B. Wang, W. Li, H.-K. Song, S. Park, R.S. Ruoff, Folding graphene film yields high areal energy storage in lithium-ion batteries, ACS Nano 12 (2) (2018) 1739–1746.
[155] C. Vaalma, D. Buchholz, M. Weil, S. Passerini, A cost and resource analysis of sodium-ion batteries, Nat. Rev. Mater. 3 (2018) 18013.
[156] S. Wang, F. Gong, S. Yang, J. Liao, M. Wu, Z. Xu, C. Chen, X. Yang, F. Zhao, B. Wang, Y. Wang, X. Sun, Graphene oxide-template controlled cuboid-shaped high-capacity VS4 nanoparticles as anode for sodium-ion batteries, Adv. Funct. Mater. 28 (34) (2018) 1801806.
[157] T. Wei, M. Zhang, P. Wu, Y.-J. Tang, S.-L. Li, F.-C. Shen, X.-L. Wang, X.-P. Zhou, Y.-Q. Lan, POM-based metal-organic framework/reduced graphene oxide nanocomposites with hybrid behavior of battery-supercapacitor for superior lithium storage, Nano Energy 34 (2017) 205–214.
[158] J.T. Robinson, F.K. Perkins, E.S. Snow, Z. Wei, P.E. Sheehan, Reduced graphene oxide molecular sensors, Nano Lett. 8 (10) (2008) 3137–3140.
[159] V. Dua, S.P. Surwade, S. Ammu, S.R. Agnihotra, S. Jain, K.E. Roberts, S. Park, R.S. Ruoff, S.K. Manohar, All-organic vapor sensor using inkjet-printed reduced graphene oxide, Angew. Chem. 122 (12) (2010) 2200–2203.
[160] C. Gómez-Navarro, R.T. Weitz, A.M. Bittner, M. Scolari, A. Mews, M. Burghard, K. Kern, Electronic transport properties of individual chemically reduced graphene oxide sheets, Nano Lett. 7 (11) (2007) 3499–3503.
[161] J. Xu, K. Wang, S.-Z. Zu, B.-H. Han, Z. Wei, Hierarchical nanocomposites of polyaniline nanowire arrays on graphene oxide sheets with synergistic effect for energy storage, ACS Nano 4 (9) (2010) 5019–5026.
[162] X. Zhu, Y. Zhu, S. Murali, M.D. Stoller, R.S. Ruoff, Nanostructured reduced graphene oxide/Fe2O3 composite as a high-performance anode material for lithium ion batteries, ACS Nano 5 (4) (2011) 3333–3338.
[163] Y. Li, W. Gao, L. Ci, C. Wang, P.M. Ajayan, Catalytic performance of Pt nanoparticles on reduced graphene oxide for methanol electro-oxidation, Carbon 48 (4) (2010) 1124–1130.
[164] M. Nawaz, W. Miran, J. Jang, D.S. Lee, One-step hydrothermal synthesis of porous 3D reduced graphene oxide/TiO2 aerogel for carbamazepine photodegradation in aqueous solution, Appl. Catal. B Environ. 203 (2017) 85–95.